J. Fluid Mech. (2010), *vol.* 657, *pp.* 189–226. © Cambridge University Press 2010
doi:10.1017/S0022112010001394

Polymer-laden homogeneous shear-driven turbulent flow: a model for polymer drag reduction

ASHISH ROBERT[1], T. VAITHIANATHAN[2]†,
LANCE R. COLLINS[2] AND JAMES G. BRASSEUR[1]‡

[1]Department of Mechanical and Nuclear Engineering, The Pennsylvania State University, 205 Reber Building, University Park, PA 16802, USA

[2]Sibley School of Mechanical and Aerospace Engineering, Cornell University, 105 Upson Hall, Ithaca, NY 14853, USA

(Received 18 February 2009; revised 15 March 2010; accepted 15 March 2010;
first published online 28 June 2010)

Drag reduction (DR) under a turbulent boundary layer implies the suppression of turbulent momentum flux to the wall, a large-eddy phenomenon. Our hypothesis is that the essential mechanisms by which dilute concentrations of long-chain polymer molecules reduce momentum flux involve only the interactions among turbulent velocity fluctuations, polymer molecules and mean shear. Experiments indicate that these interactions dominate in a polymer-active 'elastic layer' outside the viscous sublayer and below a Newtonian inertial layer in a polymer-laden turbulent boundary layer. We investigate our hypothesis by modelling the suppression of momentum flux with direct numerical simulation (DNS) of homogeneous turbulent shear flow (HTSF) and the finite extensible nonlinear elastic with Peterlin approximation (FENE-P) model for polymer stress. The polymer conformation tensor equation was solved using a new hyperbolic algorithm with no artificial diffusion. We report here on the equilibrium state with fixed mean shear rate S, where progressive increases in non-dimensional polymer relaxation time We_S (shear Weissenberg number) or concentration parameter $1-\beta$ produced progressive reductions in Reynolds shear stress, turbulence kinetic energy and turbulence dissipation rate, concurrent with increasing polymer stress and elastic potential energy. The changes in statistical variables underlying polymer DR with $1-\beta$, We_S, $\%DR$ and polymer-induced changes to spectra are similar to experiments in channel and pipe flows and show that the experimentally measured increase in normalized streamwise velocity variance is an indirect consequence of DR that is true only at lower DR. Comparison of polymer stretch and elastic potential energy budgets with channel flow DNS showed qualitative correspondence when distance from the wall was correlated to We_S. As We_S increased, the homogeneous shear flow displayed low-DR, high-DR and maximum-DR (MDR) regimes, similar to experiments, with each regime displaying distinctly different polymer–turbulence physics. The suppression of turbulent momentum flux arises from the suppression of vertical velocity fluctuations primarily by polymer-induced suppression of slow pressure–strain rate correlations. In the high-Weissenberg-number MDR-like limit, the polymer nearly completely blocks Newtonian inter-component energy transfer to vertical velocity fluctuations and turbulence is maintained by the

---

† Present address: Clear Science Corporation, 663 Owego Hill Road, Harford, NY 13784-0233, USA.

‡ Email address for correspondence: brasseur@psu.edu

polymer contribution to pressure–strain rate. Our analysis from HTSF with the FENE-P representation of polymer stress and its comparisons with experimental and DNS studies of wall-bounded polymer–turbulence supports our central hypothesis that the essential mechanisms underlying polymer DR lie directly in the suppression of momentum flux by polymer–turbulence interactions in the presence of mean shear and indirectly in the presence of the wall as the shear-generating mechanism.

1. Introduction

The discovery by Toms (1949) that the addition of long-chain polymer molecules at low concentration (a few weight parts per million) to turbulent pipe flow can reduce drag up to 80 % introduced questions that remain unresolved 60 years later. Numerous experimental, numerical and theoretical studies have shed light on the mechanism underlying drag reduction (DR). Past reviews by Lumley (1969), Liaw, Zakin & Patterson (1971), Hoyt (1971), Landahl (1973) and Virk (1975) summarize various aspects of polymer DR. Later reviews by McComb (1990), Gyr & Bewersdorff (1995), Nieuwstadt & den Toonder (2001) and White & Mungal (2008) expand on the early reviews in light of the more recent findings.

Two phenomenologies are often invoked to explain different aspects of polymer–turbulence interactions and DR. The first, proposed by Lumley (1969, 1973), was based on the enhancement of an effective extensional viscosity, leading to a displacement of the log layer away from the wall and lower wall stress. The second phenomenology, a theory proposed by Tabor & de Gennes (1986) and de Gennes (1990), was based on the 'elastic' rather than the 'viscous' properties of polymer–turbulence interactions in homogeneous turbulence, leading to a second mechanism for the transfer from turbulent to thermal energy.

Earlier experimental pipe flow results are summarized in Virk (1975). In recent years, laser Doppler velocimetry (LDV) measurements in channel flow (Willamarth, Wei & Lee 1987; Walker & Tiederman 1990; Harder & Tiederman 1991; Wei & Willamarth 1992; Warholic, Massah & Hanratty 1999) and pipe flow (Pinho & Whitelaw 1990; den Toonder *et al.* 1997; Ptasinski *et al.* 2001) have provided more details of different aspects of the DR phenomenon. More recently, advances in computational power and the development of more sophisticated constitutive models for the polymeric contribution to local stress have facilitated direct numerical simulation (DNS) of drag reducing turbulent flows. DNS accuracy is limited by the model for polymer stress, inability to resolve all relevant polymer scales and numerical instability. However, DNS has the advantage of describing the average orientation of the polymer micro-structure in relationship to the velocity field, providing additional insight into the mechanisms responsible for low versus high DR and the maximum DR (MDR) limit. With DNS it is possible to isolate the effects of the Weissenberg number, polymer concentration and maximum polymer length. The majority of DNS studies have been on polymer-laden turbulent channel flows (Sureshkumar & Beris 1995, 1997; Sureshkumar, Beris & Handler 1997; Dimitropoulos, Sureshkumar & Beris 1998; Dimitropoulos *et al.* 2001; Ilg *et al.* 2002; Min, Yoo & Choi 2003*a*; Min *et al.* 2003*b*; Ptasinski *et al.* 2003; Dubief *et al.* 2004; Dimitropoulos *et al.* 2005). A few DNS studies have been carried out on homogeneous isotropic and shear turbulent flows with polymer (Vaithianathan & Collins 2003; de Angelis *et al.* 2005; Vaithianathan *et al.* 2006, 2007). All these DNS studies have applied the finite extensible nonlinear elastic with Peterlin approximation (FENE-P) model (§ 2) for the polymer stress, which has been shown to yield good qualitative (even semi-quantitative) agreement with experimental measurements of polymer-laden wall-bounded turbulence, despite its well-known inability to reproduce the hysteresis effect in transient flows (Keunings 1997). This may be due to the fact that highly elastic polymers tend to remain stretched for long periods of time and only rarely undergo the coil–stretch transition, where the FENE-P approximation introduces the largest errors (Jin & Collins 2007).

With DNS of channel flow, Dimitropoulos *et al.* (2001), through the Reynolds stress budgets, concluded that the suppression of pressure–strain rate inter-component energy transfer was essential to DR. A similar conclusion had been suggested a decade earlier by Walker & Tiederman (1990) with channel flow experiments. Ptasinski *et al.* (2003) performed DNS of the minimal channel at the MDR limit that also points to the importance of pressure–strain rate inter-component energy transfer. Min *et al.* (2003*b*) studied the polymer elastic energy budget in channel flow. (We use the term 'elastic energy' to imply the potential energy stored within the polymer chain during stretch or potential energy released during contraction.) Their DNS suggested that the polymer stores the elastic energy from the flow very near the wall. They found that when the relaxation time is short, the elastic energy is re-released near the wall and there is no DR. However, when the relaxation time is sufficiently long, and DR occurs, the stretched polymer is transported into the inertial layer before elastic energy is released. Dubief *et al.* (2004) analysed polymer work and its interaction with the near-wall vortices in DNS of channel flow. They argued that the large fluctuations in polymer work energize streamwise velocity fluctuations in high-speed streaks above the viscous sublayer and enhance streamwise velocity fluctuations. Ptasinski *et al.* (2003), however, attributed the enhancement of streamwise velocity fluctuations to the suppression of pressure–strain rate correlations. Channel and pipe flow experiments have shown that this enhancement is suppressed at higher DR (§ 5).

The majority of the DNS studies consider the structure of the boundary layer, including the presence of the wall, the viscous sublayer and the coherent structures that exist near the wall, to be essential to the process of DR. We, however, hypothesize that the essential mechanisms that underlie the suppression of momentum transport to the wall by polymer, and therefore DR, arise from interactions among mean shear, turbulence and polymer within an 'elastic layer', and without any direct influence of the viscous sublayer.

The term 'elastic layer' originated with Virk (1971*b*, 1975), who measured a polymer-induced log layer between the viscous sublayer and a second, Newtonian, log layer that increases in depth with increasing polymer concentration. We use the term 'elastic layer' consistent with current understanding that the elastic layer is an inertial wall layer outside the viscous wall layer (if it exists) that satisfies the law of the wall with a 'von Kármán constant' that is different from the Newtonian value (e.g. L'vov *et al.* 2004). In a rough-wall polymer boundary layer where the viscous sublayer is within the roughness elements, the elastic layer presumably extends to the roughness elements.

If our hypothesis is correct, then the essential mechanisms of polymer DR should be contained within a polymer-laden homogeneous turbulent shear flow (HTSF) without a wall as a model of the suppression of momentum flux through the polymer-active elastic wall layer above the viscous layer and below the Newtonian inertial log layer. Our objectives are first to show that the DNS of polymer-laden HTSF has the same characteristics as drag reducing polymer-laden wall flows and then to analyse essential statistical characteristics associated with DR from the homogeneous shear flow DNS.

It is well known that in high-Reynolds-number wall-bounded flows of Newtonian fluids, the inertial wall layer, where influences from outer scale eddies are weak, is locally quasi-homogeneous. As a consequence, turbulence within this layer has a remarkable similarity to the turbulence in HTSF in equilibrium and at an appropriately chosen shear rate. For example, Lee, Kim & Moin (1990) compared DNS of HTSF with earlier channel flow simulations and found similarity in the statistics as well as the streaky structure of the two flows, leading them to hypothesize a certain degree of universality among all shear flows. A similar conclusion was drawn by Rogers & Moin (1987), who compared HTSF simulations with the channel flow simulations by Kim & Moin (1986) and found the vorticity fields to be structurally similar. Perhaps the most comprehensive comparison between HTSF and wall-bounded flows was carried out by Khanna (1995). In his PhD thesis, Khanna compared statistics measured experimentally in a boundary layer, HTSF simulations from a variety of sources and wind tunnel experiments by Tavoularis and coworkers that approximate HTSF. Khanna found quantitative agreement between the probability density functions (p.d.f.s) for velocity components in HTSF with the equivalent statistics in a turbulent boundary layer at $y^+ = 300$–500. He also found systematic ‘disagreement’ between the HTSF statistics and the statistics in the outer layer ($y^+ > 2000$), leading him to conclude that there are universal aspects to all shear flows when comparisons are made in the parts of the flow not strongly influenced by the wall or outer boundaries. Comparisons of pressure–velocity statistics showed a similar trend. George, Beuther & Arndt (1984) compared theory for the pressure field in HTSF with experimental measurements in a turbulent jet and found them to be in quantitative agreement. Kim & Lee (1989) compared p.d.f.s of the rapid and slow pressure–strain terms in DNS of a channel flow at $y^+ = 50$ with HTSF and found them to be in very good agreement. More modern literature has continued to build on the premise that shear flows not directly influenced by boundaries share universal structure and dynamics. For example, Casciola *et al.* (2005) discuss a ‘universal regime’ for shear flows and this universality provides the theoretical underpinnings for an analysis of the von Kármán constant in a turbulent boundary layer by Lo *et al.* (2005).

The collective evidence suggests that HTSF is an excellent model for the inertial surface layer in wall-bounded turbulent flows; inhomogeneities are weak and of secondary importance. In this study, we postulate the existence of a similar correspondence between the elastic layer of wall-bounded non-Newtonian turbulence and HTSF of non-Newtonian turbulence at a suitably chosen shear rate (non-dimensionalized with polymer relaxation time, § 2.1). We support our argument with detailed comparisons of polymer HTSF simulations with experimental measurements and DNS of channel flows in the literature. We hypothesize that although viscid–inviscid interactions between the viscous wall layer and the inertia-dominated elastic wall layer undoubtedly affect DR, the elastic layer is the primary source of the suppression of momentum flux to the surface that underlies DR, and therefore HTSF can provide new insight into the underlying mechanisms of DR.

Our hypothesis that polymer DR originates in the elastic layer is motivated, in part, by experiment. McComb & Rabie (1979, 1982) experimentally investigated the location in the turbulent boundary layer where active polymer–turbulence interactions initiate DR. They carefully followed the diffusion of polymer injected at the pipe centre and at the wall and concluded that DR initiated when the polymer entered the region $15 \leqslant y^+ \leqslant 100$, from above or below, suggesting that the dominant polymer–turbulence interactions underlying DR centre on the elastic layer between the viscous wall layer and the Newtonian inertial log layer. Within this elastic layer, both the Reynolds shear stress and the total stress (Reynolds + polymer stress) are reduced with DR. Furthermore, because the same levels of DR have been measured over rough and smooth surfaces (Spangler 1969; Virk 1971*a*), the essential mechanisms underlying DR do not require the existence of a viscous sublayer. Thus, it is reasonable to hypothesize that DR originates essentially in the dynamics of polymer–turbulence interactions with shear in the elastic layer of the turbulent boundary layer and that mechanisms associated with the viscous sublayer are secondary to the suppression of momentum flux through the elastic layer, and therefore to lower surface shear stress and DR.

Since the lower margins of the inertia-dominated wall layer have the highest levels of both turbulent fluctuations and mean shear in the presence of polymer, we argue that the essential mechanisms of polymer–turbulence DR lie in the suppression of turbulent momentum flux by polymer–turbulence dynamics in the presence of shear. We apply DNS of polymer-laden HTSF as a model for the elastic layer to explore the essential mechanisms of polymer–turbulence DR. In the present study, we analyse these mechanisms statistically and compare HTSF with channel and pipe flow experiments and channel flow simulations to validate HTSF as a model for the elastic layer of the polymer-laden drag reducing turbulent boundary layer.

2. The FENE-P model system for polymer-laden turbulent flows

Polymer-laden turbulent flow is modelled as an incompressible continuum with total stress $\tilde{\tau}_{ij}$ given by the summation of a Newtonian solvent stress $\tilde{\tau}^s_{ij}$ and polymer-induced stress $\tilde{\tau}^p_{ij}$:

$$\frac{\partial \tilde{u}_i}{\partial x_i} = 0, \tag{2.1}$$

$$\frac{\partial \tilde{u}_i}{\partial t} + \tilde{u}_j \frac{\partial \tilde{u}_i}{\partial x_j} = -\frac{1}{\rho}\frac{\partial \tilde{p}}{\partial x_i} + \frac{1}{\rho}\frac{\partial}{\partial x_j}\left(\tilde{\tau}^s_{ij} + \tilde{\tau}^p_{ij}\right), \tag{2.2}$$

where $\tilde{\tau}^s_{ij} = 2\mu_s \tilde{s}_{ij}$, with $\tilde{s}_{ij}$ being the strain rate tensor and μ_s the Newtonian viscosity of the solvent. The FENE-P dumbbell model is applied to polymer stress, $\tilde{\tau}^p_{ij}$ (Bird *et al.* 1987).

FENE molecules are modelled as two beads (neglecting their accelerations) with a nonlinear finitely extensible elastic spring in between (Bird *et al.* 1987; Larson 1999). With this model, only the longest polymer time scale is captured, the characteristic time for relaxation of polymer molecules to an equilibrium coiled state. Driven from equilibrium by fluid strain, the tendency for the polymer molecules to return to equilibrium is modelled with a nonlinear spring force that generates extra stress on the flow. The polymer stress depends on the deviation in ‘polymer conformation’ $\tilde{c}_{ij}$ from equilibrium, with polymer relaxation time scale λ_p:

$$\tilde{\tau}^p_{ij} = \frac{\mu_p}{\lambda_p}\left(f(\tilde{r})\tilde{c}_{ij} - \delta_{ij}\right). \tag{2.3}$$

The conformation tensor

$$\tilde{c}_{ij} = \langle \hat{R}_i \hat{R}_j \rangle / \frac{\langle \hat{R}^2 \rangle_{eq}}{3} \tag{2.4}$$

is defined as the local ensemble average of the dyadic product of the separation vector between the two beads of the dumbbell $\hat{R}_i$ with itself, non-dimensionalized by 1/3 the square of the average polymer length in equilibrium. Angle brackets represent an ensemble average over the configuration space of the dumbbell. The nonlinear spring force $f(\tilde{r})$ maintains finite extensibility and is specified with the following form proposed by Warner (1972):

$$f(\tilde{r}) = \frac{L^2 - 3}{L^2 - \tilde{r}^2}, \tag{2.5}$$

where $\tilde{r} = \sqrt{\tilde{c}_{ii}}$ is the polymer stretch at (x_i, t) and L is the maximum polymer length, both non-dimensionalized as per (2.4). The Peterlin (1966) approximation replaces $\langle f(\tilde{r})\hat{R}_i\hat{R}_j\rangle$ by $f(\tilde{r})\langle\hat{R}_i\hat{R}_j\rangle$ in the constitutive relation for polymer stress in (2.3). FENE models assume no polymer–polymer interactions and a nonlinear relationship between polymer stress and polymer conformation (see (2.3)). Thus, FENE models are restricted to low concentrations and cannot model polymer entanglement.

Polymer concentration is parametrized through a polymer viscosity, μ_p, where the zero-shear mixture viscosity (μ) is written as the sum of polymer (μ_p) and solvent (μ_s) viscosities, $\mu = \mu_p + \mu_s$. The ratio of solvent to mixture viscosity is defined as $\beta = \mu_s/\mu$, so that $\mu_p = (1-\beta)\mu \approx nkT\lambda_p$, where n is the polymer concentration, k is the Boltzmann constant and T is the temperature (Bird *et al.* 1987). For fixed relaxation time λ_p and noting that for a dilute polymer solution, the zero-shear solution viscosity is minimally altered by the addition of a polymer, the parameter $1-\beta$ is proportional to the polymer concentration n, and thus is considered a concentration parameter.

In the FENE-P model, polymer conformation evolves through a transport equation (Bird *et al.* 1987):

$$\frac{\partial \tilde{c}_{ij}}{\partial t} + \tilde{u}_k \frac{\partial \tilde{c}_{ij}}{\partial x_k} = \tilde{c}_{ik}\frac{\partial \tilde{u}_j}{\partial x_k} + \tilde{c}_{jk}\frac{\partial \tilde{u}_i}{\partial x_k} - \frac{1}{\mu_p}\tilde{\tau}^p_{ij}. \tag{2.6}$$

The polymer is stretched by strain rate and rotated by vorticity, given by the first two right-hand-side terms of (2.6). At high Reynolds numbers, fluctuating strain rate and vorticity are concentrated at the smallest most dissipative turbulence scales. The restoration term in (2.6) contains the nonlinear spring force $f(\tilde{r})$, which diverges as $\tilde{r} \to L$ so as to maintain finite extensibility.

We focus on the dynamics controlling alterations in momentum flux and energetics from the addition of a polymer. To this end, we apply the Reynolds decomposition with the notation $\tilde{a} = A + a$, where a variable $\tilde{a}$ is written as the sum of its ensemble mean A and fluctuation a. The components of the Reynolds stress tensor $\langle u_i u_j\rangle$ for a homogeneous shear flow with mean velocity $(U, 0, 0)$ and mean shear $S = \mathrm{d}U/\mathrm{d}y$ are given by

$$\frac{\mathrm{d}\langle u^2\rangle}{\mathrm{d}t} = -2S\,\langle uv\rangle + \phi^t_{11} - \epsilon_{11} - \Gamma_{11}, \tag{2.7}$$

$$\frac{\mathrm{d}\langle v^2\rangle}{\mathrm{d}t} = \phi^t_{22} - \epsilon_{22} - \Gamma_{22}, \tag{2.8}$$

$$\frac{\mathrm{d}\langle w^2\rangle}{\mathrm{d}t} = \phi^t_{33} - \epsilon_{33} - \Gamma_{33}, \tag{2.9}$$

$$\frac{\mathrm{d}}{\mathrm{d}t}(-\langle uv\rangle) = S\langle v^2\rangle - \phi^t_{12} + \epsilon_{12} + \Gamma_{12}, \tag{2.10}$$

where u and v are the velocity fluctuations in the mean flow (streamwise) and mean flow gradient (vertical) directions, and w are spanwise fluctuations. The Reynolds shear stress in (2.10) has been purposely written with opposite sign to facilitate the discussion of change in magnitude of turbulence momentum flux ($-\rho\langle uv\rangle$) by the polymer.

The diagonal terms in the total pressure–strain rate correlations, $\phi^t_{ij} = 2\langle p s_{ij}\rangle/\rho$, are responsible for inter-component energy transfer. There are three contributions to pressure–strain associated with 'slow' (p^s), 'rapid' (p^r) and 'polymer' (p^p) contributions to pressure fluctuations from the Poisson equation:

$$p = p^s + p^r + p^p, \tag{2.11}$$

where

$$\nabla^2 p^s = -\rho \frac{\partial^2}{\partial x_i \partial x_j}(u_i u_j), \nabla^2 p^r = -2\rho S s_{12}, \nabla^2 p^p = \frac{\partial^2}{\partial x_i \partial x_j}\tau^p_{ij}. \tag{2.12}$$

Correspondingly, the pressure–strain rate correlations contain slow (ϕ^s_{ij}), rapid (ϕ^r_{ij}) and polymer (ϕ^p_{ij}) contributions. Since the trace of the pressure–strain rate tensor is zero to maintain incompressibility, the normal pressure–strain rate correlations are responsible for the redistribution of turbulent kinetic energy (TKE) from $\langle u^2\rangle$ to $\langle v^2\rangle$ and $\langle w^2\rangle$ (see (2.7)–(2.9)). In § 7 we shall show that at high DR, polymer–turbulence interactions have a dramatic influence on the inter-component energy transfer through pressure–strain rate correlations and also these polymer-induced changes ultimately force a reduction in Reynolds shear stress. We also show that the new polymer pressure–strain rate contribution ϕ^p_{ij} plays a key role in the MDR limit.

The variable ϵ_{ij} is the viscous dissipation rate tensor, $\epsilon_{ij} = 2\nu_s\langle s_{ik}s_{kj}\rangle$, and Γ_{ij} quantifies polymer–turbulence interactions:

$$\Gamma_{ij} = \frac{1}{\rho}\left\langle \tau^p_{ik}\frac{\partial u_j}{\partial x_k} + \tau^p_{jk}\frac{\partial u_i}{\partial x_k}\right\rangle, \tag{2.13}$$

where $\tilde{\tau}^p_{ij} = T^p_{ij} + \tau^p_{ij}$. The diagonal elements of Γ_{ij} quantify the net rate of component energy transfer from TKE to polymer elastic energy. The budget for TKE, $q^2/2 = (\langle u^2\rangle + \langle v^2\rangle + \langle w^2\rangle)/2$, for HTSF is given by

$$\frac{\mathrm{d}}{\mathrm{d}t}\left(\frac{q^2}{2}\right) = -S\langle uv\rangle - \epsilon - \Gamma, \tag{2.14}$$

where $\epsilon = \epsilon_{ii}/2$ is the viscous dissipation rate of turbulence energy and $\Gamma = \Gamma_{ii}/2$ is the net rate of energy transfer from the turbulence to the polymer.

The budget equations for mean conformation tensor C_{ij} in a homogeneous shear flow are given by

$$\frac{\mathrm{d}C_{11}}{\mathrm{d}t} = 2SC_{12} + \Lambda_{11} - \frac{1}{\mu_p}T^p_{11}, \tag{2.15}$$

$$\frac{\mathrm{d}C_{22}}{\mathrm{d}t} = \Lambda_{22} - \frac{1}{\mu_p}T^p_{22}, \tag{2.16}$$

$$\frac{\mathrm{d}C_{33}}{\mathrm{d}t} = \Lambda_{33} - \frac{1}{\mu_p}T^p_{33}, \tag{2.17}$$

$$\frac{\mathrm{d}C_{12}}{\mathrm{d}t} = SC_{22} \ + \Lambda_{12} - \frac{1}{\mu_p}T^p_{12}, \tag{2.18}$$

where $\tilde{c}_{ij} = C_{ij} + c_{ij}$. Mean polymer stretch $R^2 = C_{ii}$ evolves according to

$$\frac{\mathrm{d}R^2}{\mathrm{d}t} = 2SC_{12} + \Lambda_{kk} - \frac{1}{\mu_p}T^p_{kk}. \tag{2.19}$$

The terms containing mean shear S in (2.15)–(2.18) and (2.19) describe the mean rate of stretch and reorientation of polymer by mean shear. Λ_{ij} describes the rates at which the polymer is stretched and rotated by fluctuating strain rate and vorticity:

$$\Lambda_{ij} = \left\langle c_{ik}\frac{\partial u_j}{\partial x_k} + c_{jk}\frac{\partial u_i}{\partial x_k}\right\rangle. \tag{2.20}$$

The net rate of polymer stretch Λ_{kk} in (2.19) involves only strain rate fluctuations. The mean restoration terms (last terms in (2.15)–(2.18) and (2.19)) maintain finite extensibility in the mean.

When the polymer is stretched by the turbulence, energy passes from the turbulence to the polymer where it adds to the polymer elastic energy E_p. Conversely, as the polymer relaxes, elastic energy passes back to the turbulence from the polymer. The net rate of energy transfer to the polymer from turbulence is given by Γ. Mean polymer elastic energy and its budget are given for HTSF by

$$E_p = -\frac{\mu_p(L^2-3)}{2\rho\lambda_p}\left\langle \ln\left(1-\frac{\tilde{r}^2}{L^2}\right)\right\rangle, \tag{2.21}$$

where

$$\frac{\mathrm{d}E_p}{\mathrm{d}t} = \frac{1}{\rho}T_{12}^{p}S + \Gamma - \frac{1}{2\rho\lambda_p}\left\langle\frac{\tilde{\tau}_{ii}^{p}}{1-\tilde{r}^2/L^2}\right\rangle = P_p + \Gamma - \epsilon_p. \tag{2.22}$$

The first right-hand-side term in (2.22) quantifies the rate of increase in polymer elastic energy due to stretching from the mean shear S (production P_p). As discussed, Γ is the net transfer of energy to/from the polymer from/to the turbulence, Γ. In addition, however, energy can flow from the polymer to fluid internal energy, as described by the last right-hand-side term in (2.22). In principle, this addition to thermal energy takes place at the polymer scale, well below the turbulence eddy scales. Thus, the addition of a polymer to the flow produces a second route from turbulent energy to fluid internal energy (polymer dissipation ϵ_p) in addition to Newtonian viscous dissipation.

2.1. *Important dimensionless parameters for comparison between homogeneous shear and channel or boundary layer flows*

The important dimensionless parameters to compare a homogeneous shear flow with the channel or boundary layer flows can be obtained from (2.2) normalized with the characteristic mean time scale S^{-1}, the turbulent velocity scale q and the mixing length scale q/S. Pressure is normalized by ρq^2 and we scale the conformation tensor $\tilde{c}_{ij}$ appearing in polymer stress (see (2.3)) by L^2 to produce

$$\frac{\partial u_i^*}{\partial t^*} + u_j^*\frac{\partial u_i^*}{\partial x_j^*} = -\frac{\partial p^*}{\partial x_i^*} + \frac{\beta}{Re_S}\frac{\partial \tau_{ij}^{s*}}{\partial x_j^*} + \frac{(1-\beta)L^2}{We_S Re_S}\frac{\partial \tau_{ij}^{p*}}{\partial x_j^*}, \tag{2.23}$$

where $*$ denotes non-dimensional quantities. $Re_S = q(q/S)/\nu = q^2/\nu S$ is a large-scale Reynolds number and $We_S = \lambda_p/S^{-1}$ is a Weissenberg number, the ratio of polymer relaxation time to the mean shear time scale. Equation (2.23) suggests that four important dimensionless parameters must be matched between a homogeneous shear flow and the boundary layer or channel flows for a proper comparison: Reynolds number Re_S, Weissenberg number We_S, maximum polymer stretch non-dimensionalized by the equilibrium length L and concentration parameter $1-\beta$.

Note that in boundary layer studies, the Weissenberg number is often defined as $We_\tau = \lambda_p u_\tau^2/\nu = \lambda_p S_o$, where u_τ is the friction velocity and S_o is the mean shear rate

Cases	λ_p	We_S	We_η	β	$\tilde{r}_o^2$	Re_l	Re_λ	S^*	Re_S
N	–	–	–	–	–	833	113	12.8	65
A	0.050	1.4	3.2	0.95	28.6	791	116	13.6	58
B	0.075	2.1	4.8	0.95	46.7	762	120	15.4	49
C	0.100	2.8	6.4	0.95	66.4	720	122	17.0	42
D	0.125	3.5	8.0	0.95	87.6	677	122	18.2	37
E	0.150	4.2	9.6	0.95	110.0	619	121	18.8	33
F	0.175	5.0	11.1	0.95	135.0	587	119	19.5	30
G	0.250	7.1	16.0	0.95	216.0	454	111	19.6	23
H	0.375	10.6	24.0	0.95	377.0	308	100	19.2	16
256N	–	–	–	–	–	2653	165	12.1	219
256A	0.050	1.4	6.0	0.95	28.6	3357	208	20.6	163
256B	0.075	2.1	9.0	0.95	46.7	3413	231	27.5	124
256B1	0.075	2.1	9.0	0.90	46.7	3253	238	29.1	112
256B2	0.075	2.1	9.0	0.80	46.7	2994	246	30.6	98
256B3	0.075	2.1	9.0	0.70	46.7	2765	251	31.7	87
256D	0.125	3.5	15.0	0.95	87.6	2888	242	33.1	87
256F	0.175	5.0	21.0	0.95	135.0	2410	241	34.8	69
256F1	0.175	5.0	21.0	0.90	135.0	1995	233	33.0	60
256F2	0.175	5.0	21.0	0.80	135.0	1632	224	31.0	53
256F3	0.175	5.0	21.0	0.70	135.0	1389	215	29.4	47
256G	0.250	7.1	30.0	0.95	216.0	1940	235	35.8	54
256H	0.375	10.6	45.0	0.95	380.0	1519	226	36.7	41
256I	0.5	14.1	60.0	0.95	490.0	1316	220	37.1	35
256J	1.0	28.3	120.0	0.95	1130.0	925	203	36.5	25
256K	1.5	42.4	180.0	0.95	1750.0	772	196	36.1	21
256L	2.0	56.6	240.0	0.95	2500.0	702	194	36.2	19
256M	2.5	70.7	300.0	0.95	3500.0	672	196	36.7	18
256O	3.0	84.9	360.0	0.95	4200.0	661	197	37.2	18

TABLE 1. Parameters used for the DNS of HTSF (at $St = 8$). Note the system to identify different simulations: 256^3 simulations start with the number 256 while 128^3 simulations start with letters (e.g. N, A, B, ...). N indicates the Newtonian flow simulation. Variation with β with the same We_S is indicated by numbers following the letters (e.g. B1, B2, B3, ...). The Kolmogorov time scale in We_η is taken from the corresponding Newtonian simulation at the same St. All other parameters are defined from the polymer states.

at the wall. In our simulations S is to be compared with the local shear rate in the elastic layer. Also note that another useful Weissenberg number is $We_\eta = \lambda_p/\tau_\eta$, where τ_η is the Kolmogorov time scale in a corresponding Newtonian flow. Based on the arguments of Lumley (1969), a polymer can actively alter the turbulence only when $We_\eta \gtrsim 1$. We list both We_S and We_η for our simulations in table 1.

3. Numerical algorithm and simulations

3.1. *Numerical algorithm for the conformation tensor*

The conformation tensor $\tilde{c}_{ij}$ is symmetric and positive definite (SPD) with positive eigenvalues λ_α bounded by $\tilde{r}^2 = \tilde{c}_{ii} = \lambda_1 + \lambda_2 + \lambda_3 \leqslant L^2$. To avoid Hadamard instabilities (Dupret & Marchal 1986), the numerical algorithm for (2.6) must maintain the SPD property of $\tilde{c}_{ij}$ and satisfy the bound for $\tilde{r}^2$. The hyperbolic nature of (2.6) leads to discontinuities at the smallest resolved scales. To maintain stability, it has become common practice to introduce global or local artificial diffusivity in advancing the conformation equation (Sureshkumar & Beris 1995; Sureshkumar *et al.* 1997; Min *et al.* 2003*b*; Dubief *et al.* 2004), thus changing the mathematical form of (2.6) and suppressing small-scale polymer–turbulence dynamics. In this study, we apply the algorithm described in Vaithianathan *et al.* (2006) that was designed to maintain the SPD property of $\tilde{c}_{ij}$ and boundedness of $\tilde{c}_{ii}$ without explicit artificial diffusion.

Vaithianathan *et al.* (2006) used a generalization of the second-order central difference scheme of Kurganov & Tadmor (2000), designed to advance the scalar equation at high Schmidt number in a way that guarantees positive scalar locally and maintains the amplitude in the discontinuous jumps in scalar concentration at the grid scale. Vaithianathan *et al.* (2006) extended the algorithm to force a tensor field to remain positive definite at most points following an update. An important consequence is that the eigenvalues remain individually positive definite and bounded in the sum by L^2, and the conformation tensor is conserved in the mean. Jumps in the local values of the conformation tensor at the grid scale maintain proper magnitude with minimal numerical diffusion and no Gibbs overshoot, so that the polymer–turbulence dynamics at the smallest resolved scales are well captured. The update is of second order, except at points at which the SPD property cannot be guaranteed. At these points (less than 5 % of the grid points), the update automatically drops to first order and ensures that the SPD property is maintained throughout. This reduction in order generally corresponds to a near-discontinuity in the conformation tensor.

3.2. *The simulations*

We performed DNS of HTSF with polymer stress given by the FENE-P dumbbell model. The numerical scheme for the conformation tensor described above was implemented in a code that employed the Rogallo algorithm to predict the velocity field for a homogeneous shear flow with specified shear $S = \mathrm{d}U/\mathrm{d}y$. The algorithm was developed by Rogallo (1981) and applied by Lee (1985), Rogers & Moin (1987) and Brasseur & Lin (2005). The Rogallo algorithm solves the dynamical system in a frame of reference that deforms with the applied mean shear S, so that the periodic boundary conditions are applied to only fluctuating variables. The fluctuating velocity field is evolved pseudo-spectrally and aliasing errors are removed by truncation and phase shift. To avoid overly distorted grid cells, the grid is 'remeshed' every odd integer St value, where t is the time. Dealiasing is performed after remeshing (Rogallo 1981), resulting in a slight loss of TKE. Data are collected at even St.

The Newtonian equations were modified to include the polymer stress tensor as per (2.2). We implemented the finite difference method discussed in § 3.1 for the conformation tensor $\tilde{c}_{ij}$ in the deforming frame of reference. Newtonian homogeneous shear flow turbulence is non-stationary in the equilibrium state, with growing integral scales and with turbulent energy production rate exceeding the dissipation rate. When the streamwise integral scales grow to be of the order of the box size, the direct influence of the periodic boundary conditions on the solution precludes continued analysis of the data. Experimentation suggests that the boundary influence becomes significant when the largest integral scale exceeds $\sim L_x/10$, where L_x is the streamwise dimension of the computational box. To accommodate the streamwise growing integral scales and extend the analysis period, the computational domain was made twice as long in the streamwise direction, as is common practice (Rogers & Moin 1987; Brasseur & Lin 2005). The smallest scale that can be resolved by the grid is correspondingly twice as long in the streamwise direction. All calculations in the present study were carried out on 128^3 and 256^3 grids.

The simulations were initiated with an initial velocity spectrum chosen so that both the largest and smallest Kolmogorov scales were well resolved at the time of analysis. We emphasize the importance of good resolution of both the largest and smallest dynamically important turbulence scales because important dynamics underlying polymer–turbulence interactions occur at both the largest and smallest scales of motion. In all simulations, at least 10 integral scales spanned the box in the streamwise direction, and the Kolmogorov scales were always well resolved, with $k_{max}\eta \approx 1.15$–1.50 during the analysis periods. The velocity field was initialized with Gaussian random solenoidal fluctuations with an initial energy spectrum $E(k) \propto k^2$ up to the energy peak at $k_p = 10$, then proportional to $k^{-5/3}$ afterwards.

To evaluate the influence of systematic parameter variations, it was important to initiate polymer–turbulence interactions around $St \approx 2$, independent of the Weissenberg number We_S or concentration parameter $1 - \beta$, both to study the initiation process and so that a non-stationary equilibrium growth state would be attained before the streamwise integral scales grow too large for the box. To accomplish this, the polymer was 'pre-stretched' with uniform diagonal components of the conformation tensor $\tilde{c}_{\alpha\alpha} = \tilde{r}_o^2/3$. Off-diagonal terms of the conformation tensor were set to zero. The initial stretch was given by $\tilde{r}_o^2 = (0.001\tilde{r}_c^4 + 0.69\tilde{r}_c^2 - 5.4)/2$, where $\tilde{r}_c^2$ is a 'critical stretch', above which the polymer force competes with the viscous force. The critical stretch $\tilde{r}_c^2$ was estimated by equating polymer force and viscous force in (2.2) and scaling, to produce

$$\tilde{r}_c^2 = \frac{3\beta We_S L^2}{(1-\beta)L^2 + 3\beta We_S}. \tag{3.1}$$

A list of the simulations applied to the present study is given in table 1 along with relevant parameters. The time step is chosen small enough to satisfy the Courant condition described in Vaithianathan *et al.* (2006) so that $\tilde{c}_{ij}$ evolved in time without the loss of its SPD property. In all simulations, mean shear rate was fixed at $S = 28.3$, fluid density $\rho = 1$, maximum polymer length at $L = 100$ and solvent viscosity $\mu_s = 0.015$ for 128^3 and $\mu_s = 0.006$ for 256^3 simulations. (Note that in DNS of homogeneous turbulence, the units of dimensional parameters are arbitrary and only non-dimensional parameters (table 1) are meaningful.) The parameters listed in table 1 are defined during an estimated quasi-equilibrium shear-dominated period (below). In table 1 two Weissenberg numbers and three Reynolds numbers are tabulated. $We_\eta = \lambda_p/\tau_\eta$ is defined using the Kolmogorov time scale τ_η for the corresponding Newtonian turbulent flow at the same St. Integral and Taylor microscale Reynolds numbers, in contrast, are given in table 1 for the polymer flow itself in the quasi-equilibrium period. $Re_l \equiv q^4/\epsilon\nu_s$, where q^3/ϵ is a turbulence integral length scale, and $Re_\lambda \equiv q\lambda_{11,1}/\nu_s$, where $\lambda_{11,1}$ is the streamwise Taylor microscale and $q = \sqrt{q^2}$ is the large-eddy turbulence velocity scale. We also tabulate the shear rate parameter $S^* = Sq^2/\epsilon$ at quasi-equilibrium, the shear rate non-dimensionalized by an integral turbulence time scale q^2/ϵ. As discussed in § 2.1, Re_S is a large-eddy Reynolds number based on the mixing length q/S. Note that $Re_S = Re_l/S^*$.

In our simulations we have covered the range of Weissenberg numbers $We_S \approx 1.4$–85. As shown in figure 1, from a low- and high-DR channel flow DNS, this range of We_S is typical in a polymer-laden channel flow. The data from these channel flow DNS were kindly supplied by Drs K. D. Housiadas and A. N. Beris and will be used at several different places in our study. Details of the data can be found from Housiadas & Beris (2003, 2005).

Figure 1 shows that We_S increases towards the wall in DNS of the channel flow. The increase in We_S is particularly rapid close to the wall within the highly polymer-active 'elastic layer', $y^+ \gtrsim 15$. We shall show in §§ 6 and 8 that the polymer-laden HTSF simulations with increasing We_S are quantitatively similar to moving towards the wall

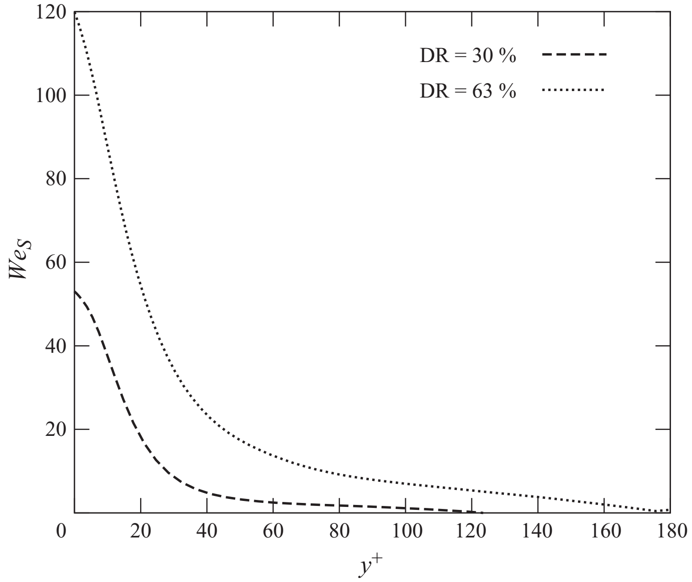

FIGURE 1. Variation of Weissenberg number We_S with y^+ in channel flow. Channel flow data used from Housiadas & Beris (2003, 2005).

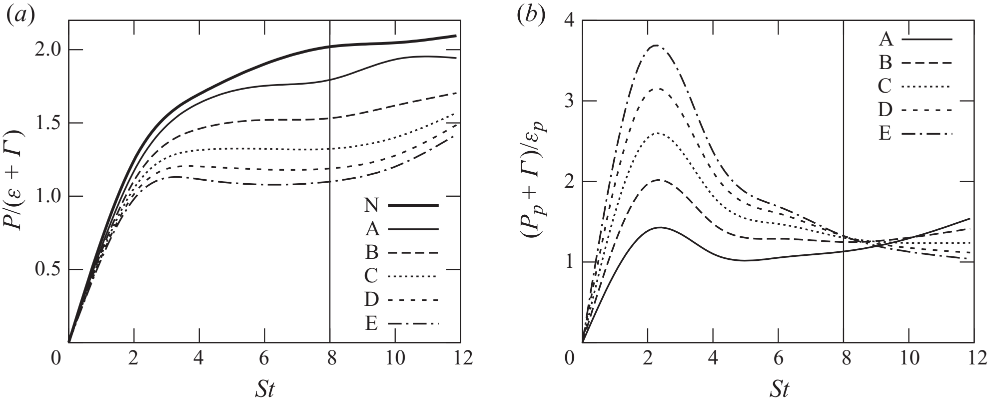

FIGURE 2. Effect of Weissenberg number We_S on the evolution of total production and total destruction rates ratios for (*a*) TKE $q^2/2$ (see (2.14)) and (*b*) elastic energy (E_p) (see (2.22)).

in a polymer-laden channel flow where the variation of We_S with y^+ is taken into account. Because increasing We_S progressively moves the polymer effect to the larger scales, at high enough We_S the largest affected scales are poorly resolved. This leads to spurious behaviour at larger We_S for low-resolution 128^3 simulations, and values of $We_S > 10$ can only be studied with high-resolution 256^3 simulations (table 1).

The non-stationary 'equilibrium' state was chosen based on the evolution of several statistics, including the ratio of total production rate to total destruction rate of TKE $q^2/2$ (see (2.14) and figure 2*a*) and polymer elastic energy E_p (see (2.22) and figure 2*b*). From these and other statistics we conclude that the turbulence moves into quasi-equilibrium when $St \geqslant 8$. Other statistics indicate that the boundary conditions begin to influence the statistics between $St \sim 10$–12. We therefore chose $St = 8$ as the 'equilibrium' time for the analysis; parameters in table 1 are tabulated at $St = 8$. In this study the level of polymer effect was systematically varied through Weissenberg

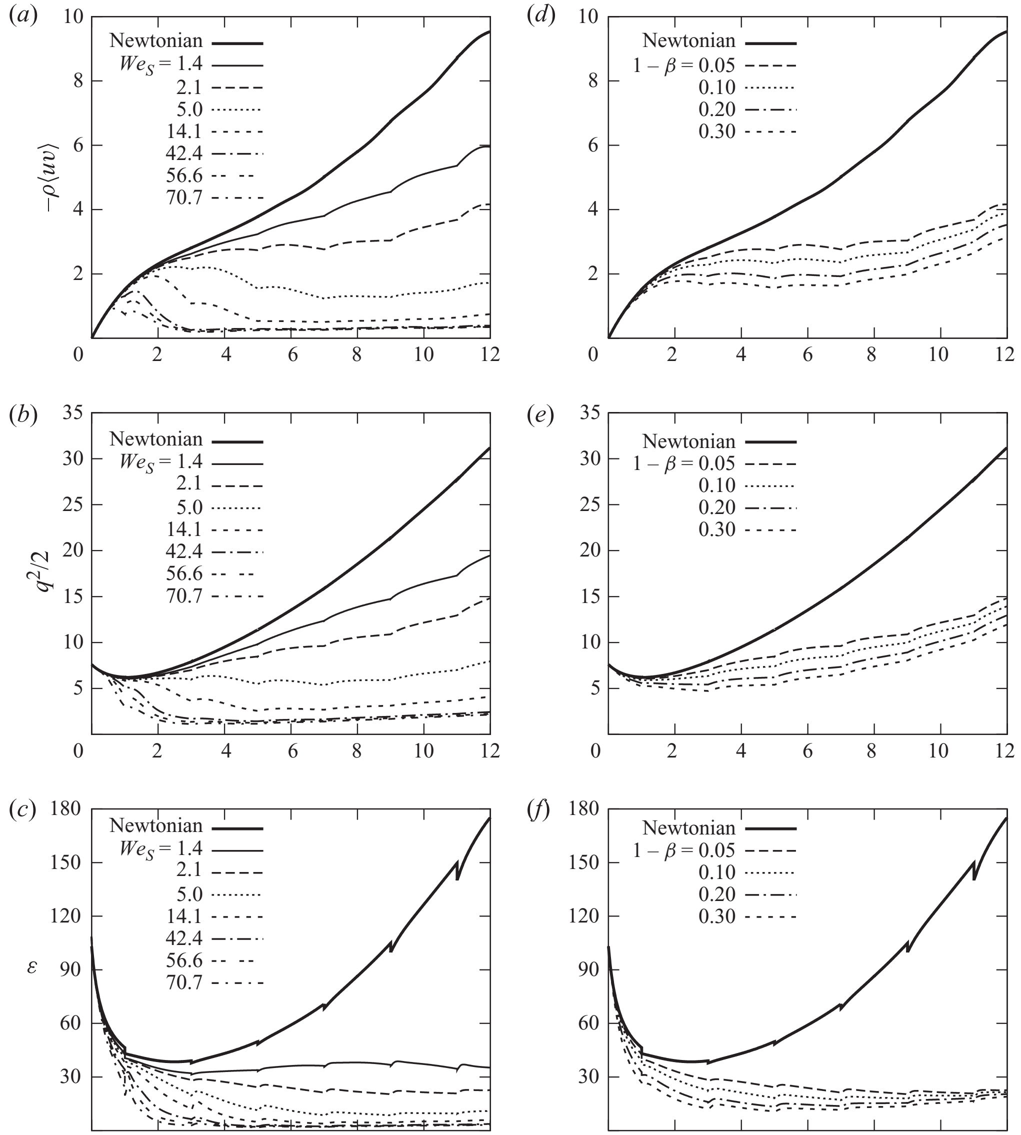

FIGURE 3. Effect of Weissenberg number We_S ($1-\beta=0.05$) (*a–c*) and polymer concentration parameter $1-\beta$ ($We_S=2.1$) (*d–f*) on Reynolds shear stress $-\rho\langle uv\rangle$ (*a*, *d*), TKE $q^2/2$ (*b*, *e*) and viscous dissipation rate ϵ (*c*, *f*). Refer to table 1 for further details of the simulations.

number $We_S \sim 1$–85 and polymer concentration $1-\beta \sim 0.05$–0.3. Maximum polymer length $L \approx 100$ is close to the value 103 given by R. G. Larson (private communication, 2006) for polyethylene oxide (PEO), with molecular weight 2×10^6.

4. Evolution of some basic polymer–turbulence interactions

Figure 3 shows the influence of polymer on the evolution of the Reynolds shear stress $-\rho\langle uv\rangle$, TKE $q^2/2$ and viscous dissipation rate ϵ. It should be noted that the ‘kinks’ at odd *St* in the curves of figures 3 and 4 are a consequence of the remeshing procedure in the Rogallo algorithm (§ 3.2). Due to the dealiasing that accompanies the remeshing step, a small amount of TKE is lost. Both Reynolds shear stress $-\rho\langle uv\rangle$ and TKE $q^2/2$ are large-scale quantities and are progressively suppressed with increasing Weissenberg number We_S (figure 3*a,b*) and polymer concentration, $1-\beta$ (figure 3*d,e*). As discussed in § 1, suppression of turbulent momentum flux $-\rho\langle uv\rangle$ underlies DR. Figure 3(*a*) shows that with increasing Weissenberg number We_S, Reynolds shear stress $-\rho\langle uv\rangle$ is suppressed rapidly initially and asymptotes to the same non-zero value when $We_S \gtrsim 40$. This result is consistent with the experiments of Warholic *et al.* (1999) and Ptasinski *et al.* (2001), who showed that the Reynolds shear stress is driven to small finite values in the MDR limit (§ 5).

Like Reynolds stress, TKE is suppressed with the addition of a polymer (figure 3*b*). When $We_S \gtrsim 5$, TKE asymptotes to values below their initial values. Figure 3(*c,f*) shows the effect of polymer on viscous dissipation rate ϵ, a small-scale quantity. Viscous dissipation rate is suppressed even more severely than Reynolds shear stress and TKE relative to the Newtonian flow. Interestingly, all three variables approach a fixed finite asymptotic value when $We_S \gtrsim 40$. Attainment of finite asymptotic values by both large- and small-scale variables at high We_S, which are independent of We_S, is conceptually similar to the MDR limit observed in experiments at large concentrations. Interestingly, figure 3(*d–f*) does not suggest a fixed point at the highest concentrations simulated. This could reflect the nature of the FENE-P model as restricted to very low concentrations.

The changes in polymer mean stretch R^2, polymer elastic energy E_p and polymer–turbulence energy exchange rate Γ are shown in figure 4(*a–c*) with increasing Weissenberg number We_S, and in figure 4(*d–f*) with increasing polymer concentration $1-\beta$. All polymer variables initially increase with time, with higher rates of increase at higher Weissenberg number and polymer concentration. However, in nearly all cases, the polymer variables eventually peak and decrease, with the peak occurring at progressively lower St with higher We_S and $1-\beta$. In most variables with a peak, the magnitude of the peak increases with increasing We_S or $1-\beta$. However, for polymer energy E_p at high We_S, the magnitude of the peak decreases with increasing We_S or $1-\beta$ (figure 4*b*). The reductions in the polymer variables are a consequence of a strong polymer-induced suppression of turbulent strain rate fluctuations at the smaller scales (figure 3*c,f*). These suppressions are more rapid at higher Weissenberg number and concentration, causing the peak in elastic energy to shift to lower St.

Mean polymer stretch R^2 behaves similarly to elastic energy with increasing We_S (figure 4*a*); the polymer is almost stretched to its maximum length and asymptotes when $We_S \gtrsim 40$, suggesting an MDR-like state. The mean polymer stretch R^2 responds to increasing polymer concentration $1-\beta$ differently from the way it responds to increasing We_S. Although R^2 increases with increasing We_S (figure 4*a*), it decreases with increasing polymer concentration (figure 4*d*). Yet polymer elastic energy increases with increasing We_S and $1-\beta$ (figure 4*e*), while Reynolds stress, TKE and viscous dissipation rate are all suppressed. This is because at larger polymer concentration, the polymer can hold significant polymer energy E_p at lower stretch, and can suppress the Reynolds stress, TKE and viscous dissipation rate with a larger number of low-level stretch events. By contrast, at higher Weissenberg numbers, the polymer effects are accomplished by fewer events involving a higher polymer stretch.

Figure 4(*c,f*) shows the evolution of turbulence–polymer energy exchange rate Γ. It is through Γ that the polymer extracts energy from the turbulence, as described by (2.22) and (2.14). Although, in principle, Γ can be of either sign, implying that energy passes in both directions, we find that the average energy exchange Γ is

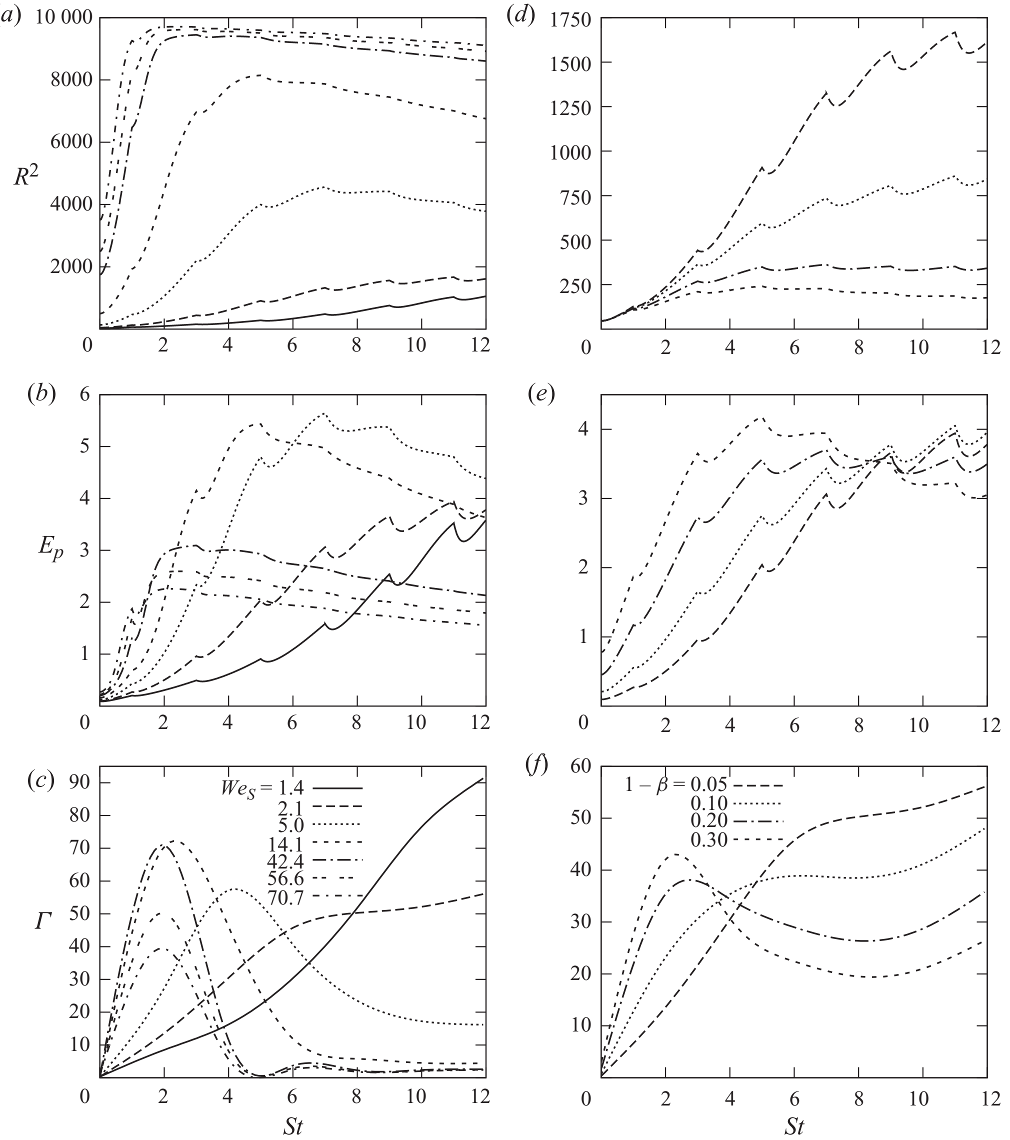

FIGURE 4. Effect of Weissenberg number We_S ($1-\beta=0.05$) (*a–c*) and polymer concentration parameter $1-\beta$ ($We_S=2.1$) (*d–f*) on polymer stretch R^2 (*a,d*), elastic energy E_p (*b,e*) and polymer–turbulence energy exchange rate Γ (*c,f*). Description for different lines shown in (*c*) is the same for (*a*) and (*b*) and similarly in (*f*) for (*d*) and (*e*). Refer to table 1 for further details of the simulations.

always from the turbulence to the polymer. We find that Γ behaves similarly to elastic energy E_p, except that it peaks earlier and decreases both with increasing Weissenberg number We_S and polymer concentration $1-\beta$. This is because the turbulence–polymer exchange rate Γ results from the small-scale strain rate acting on polymer stress (see (2.13)), and elastic energy E_p increases both from the fluctuating strain rate acting on fluctuating polymer stress (Γ) and from the mean strain rate acting on mean polymer stress (see (2.22)).

5. Comparison with the channel flow experiments

We have hypothesized (§ 1) that the polymer-laden HTSF contains the essential dynamics underlying DR. To test this hypothesis, we searched the literature for experimental data that could be compared with predictions from our HTSF simulations. We analysed in detail the experimental data of Ptasinski *et al.* (2001) in pipe flow and Warholic *et al.* (1999) in channel flow, where percentage drag reduction ($\%DR$) was reported along with statistics such as Reynolds stress tensor components plotted relative to the wall and normalized on wall friction velocity and length scales. Since both $\%DR$ and the Newtonian values were reported, it was possible to renormalize their measured statistics using the corresponding values from the Newtonian state before polymer was added for comparison with our DNS. We found that although the data of Ptasinski *et al.* and Warholic *et al.* were collected in different internal flow geometries with different polymers and at different Reynolds numbers, when plotted normalized by the Newtonian values, the Reynolds shear stress and velocity variances displayed the same variations with $\%DR$ and were even similar in value. However, the data of Warholic *et al.* are much better resolved in $\%DR$ and are more detailed for comparison with our HTSF results. We carefully re-analysed both sets of data and found that the two studies are consistent with each other. The primary difference between the data of Warholic *et al.* and the less complete data of Ptasinski *et al.* is at the highest values of $\%DR$, where Warholic *et al.* measured somewhat lower values of Reynolds stress statistics; however, the differences are not severe, as shown in figure 5(*a*), and both data sets show large reductions in $-\rho\langle uv\rangle$, $\langle u^2\rangle$ and $\langle v^2\rangle$ of 65 %–90 % at the highest measured values of DRs (64 %–70 %). In comparing these data with our simulations, whereas experimentally $\%DR$ is increased by increasing concentration, in DNS we increased $\%DR$ primarily by increasing We_S at fixed concentration parameter $1-\beta$, and secondarily by increasing $1-\beta$ at fixed We_S. In addition, it should be kept in mind that the mean shear S is held fixed in HTSF simulations, whereas S increases in the elastic layer of the boundary layer as polymer concentration increases (Virk 1971*b*, 1975).

Warholic *et al.* introduced Percol 727, a copolymer of polyacrylamide and sodium acrylamide at high concentration through a slot in the wall of a turbulent fully developed channel flow, and sampled the fluid downstream to quantify polymer concentration at the same location where data were collected. Mean velocity, Reynolds stress $-\rho\langle uv\rangle$, component kinetic energies $\langle u^2\rangle$, $\langle v^2\rangle$, u–v velocity correlation coefficient ρ_{uv} and polymer stress T_{12}^p (by subtraction) were presented in plots as functions of distance from the wall for different $\%DR$, measured as % change in wall shear stress at a fixed flow rate. From these plots, we were able to extract peak values of statistics $-\langle uv\rangle$, $\langle u^2\rangle$, $\langle v^2\rangle$, etc. near the wall as a function of $\%DR$; we used these as representative values for the polymer-active elastic layer for comparison with statistics generated in HTSF. These comparisons are made as if the flow rate were held fixed as polymer is added to the flow. Because wall shear stress approximates the total momentum flux through the elastic layer to the wall, $\%DR$ can be estimated by

$$\%DR = \frac{[-\rho\langle uv\rangle]^{Newtonian} - \left[-\rho\langle uv\rangle + T_{12}^p\right]^{Polymer}}{[-\rho\langle uv\rangle]^{Newtonian}} \times 100. \tag{5.1}$$

To validate (5.1), in figure 5(*b*) we plot $\%DR$ calculated from (5.1) using the peak values of $-\rho\langle uv\rangle$ and T_{12}^p in the elastic layer of the channel flow experiments against the $\%DR$ reported by Warholic *et al.* based on the wall shear stress measured from the pressure drop and flow rate. The correlation coefficient is $r = 0.97$, confirming

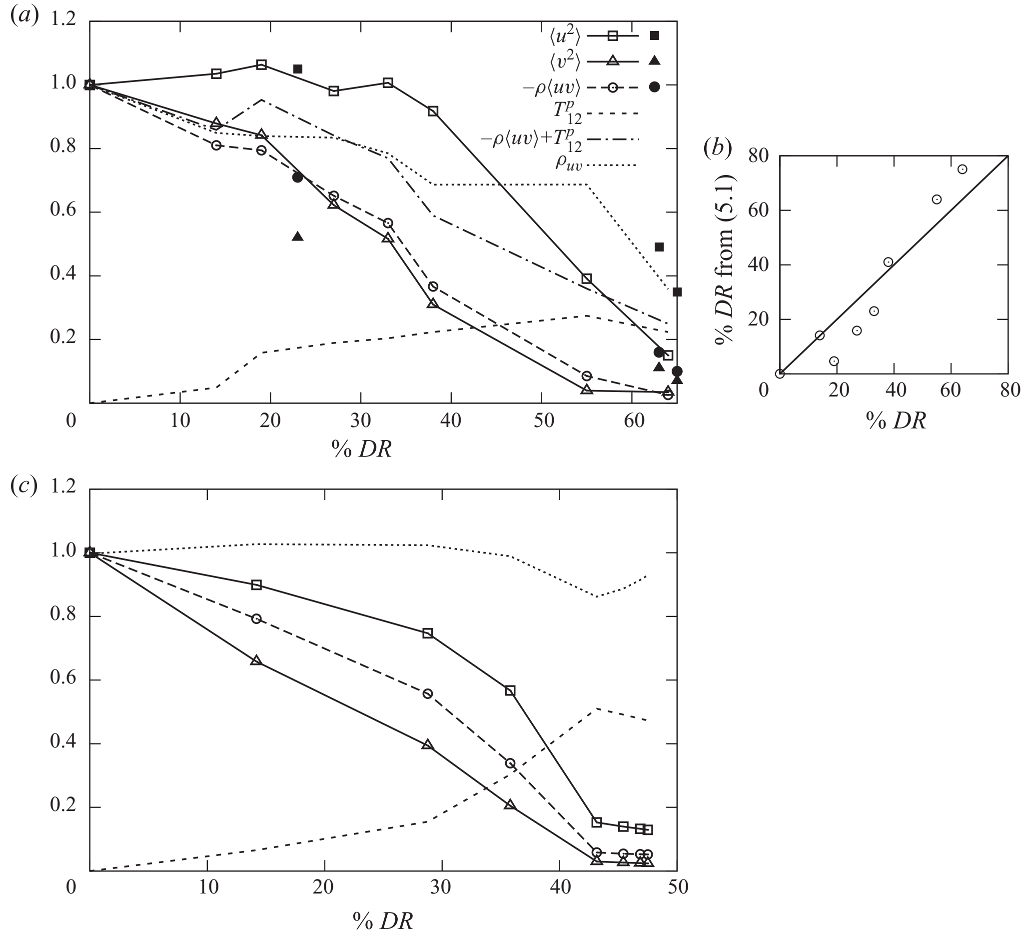

FIGURE 5. (*a*) Polymer DR channel flow experimental data replotted from Warholic *et al.* (1999) (using open symbols and lines) and pipe flow experimental data from Ptasinski *et al.* (2001) (with solid symbols). (*b*) %*DR* calculated from (5.1) with %*DR* observed in the experiments ($r = 0.97$). Data from homogeneous shear flow simulations are plotted in (*c*) with %*DR* calculated from (5.1). All numerical data are for 256^3 simulations. All data are normalized by the corresponding Newtonian values except for the polymer stress T^p_{12}, which are normalized by the Newtonian Reynolds shear stress $-\rho\langle uv \rangle$.

that the suppression in total stress $-\rho\langle uv \rangle + T^p_{12}$ within the elastic layer determines %*DR*. Since the experimental data presented by Warholic *et al.* are unique functions of %*DR*, we used (5.1) to plot statistics from polymer-laden HTSF against %*DR* to compare with the experimental data. We compare primarily with the detailed data of Warholic *et al.*, but include the less detailed data of Ptasinski *et al.*

We plot the experimental results in figure 5(*a*) with %*DR* for comparison with the HTSF plotted in figure 5(*c*). In all plots the polymer values are non-dimensionalized by the corresponding Newtonian values with the exception of T^p_{12}, which is non-dimensionalized by the Newtonian Reynolds shear stress $-\rho\langle uv \rangle$. In interpreting figure 5, it should be kept in mind that, unlike most papers on polymer DR, the statistics are not normalized by the friction velocity (which decreases with increase in %*DR*). Also note that the same line types are used in the experimental and numerical results for ease of comparison. The numerical values for total stress $-\rho\langle uv\rangle + T^p_{12}$ are not given in figure 5 (*c*), as these will be discussed in § 6.

We begin by noting from figure 5(*a*) that the data of Warholic *et al.* (open symbols and lines) and that of Ptasinski *et al.* (solid symbols) are consistent with one another. In fact, at 23 % DR the normalized Reynolds shear stress and streamwise velocity variance match, despite the fact that two experiments use different polymers and are performed in different flow geometries. Ptasinski *et al.* measure somewhat lower vertical velocity variance than Warholic *et al.* at 23 % DR. In comparison, both Ptasinski *et al.* and Warholic *et al.* measure dramatic drops in all Reynolds stress components at the highest %*DR* measured by Ptasinski *et al.* (62 %–64 %*DR*). Although Warholic *et al.* measure somewhat lower values of Reynolds stress than Ptasinski *et al.*, likely due to polymer entanglement at their highest concentrations, the differences are not severe and both sets of data show that at high DR and MDR, both Reynolds shear stress and turbulence energy are strongly suppressed in the elastic layer by polymer–turbulence interactions.

Overall, the qualitative trends are the same between the HTSF simulations and channel flow experiments. Reynolds shear stress $-\rho\langle uv\rangle$ and vertical velocity variance $\langle v^2\rangle$, in particular, are increasingly suppressed with increasing %*DR*, with the rate of suppression initially rapid and then asymptoting at high %*DR* in both the experiment and HTSF (figure 5*a,c*). Note that vertical velocity variance $\langle v^2\rangle$ is the most suppressed quantity at higher DRs in both HTSF and experiments. Because the Reynolds shear stress production is proportional to $\langle v^2\rangle$ (see (2.10)), the suppression of $\langle v^2\rangle$ leads to reduction in $-\rho\langle uv\rangle$.

The streamwise velocity variance $\langle u^2\rangle$ shows an interesting difference in figure 5 between experiments and HTSF. The shape of the curves for both experiments and HTSF with %*DR* is similar; however, in the experiments, $\langle u^2\rangle$ initially increases slightly before rapidly decreasing when %*DR* exceeds from 30 % to 40 %, while in the simulations, $\langle u^2\rangle$ decreases monotonically throughout. The initial increase in $\langle u^2\rangle$ at lower %*DR* has been observed in both experiments and simulations for channel flow. (It should, however, be noted that when $\langle u^2\rangle$ is plotted normalized by u_τ^2, as is commonly done, the increase in $\langle u^2\rangle/u_\tau^2$ is exaggerated relative to the increase in $\langle u^2\rangle$ since u_τ^2 decreases with increasing %*DR* when volume flow rate is held fixed, as was done in the experiments.) This slight increase in $\langle u^2\rangle$ occurs in channel flow because mean shear increases within the elastic layer with the addition of the polymer, increasing turbulence production of $\langle u^2\rangle$ (see (2.7)) at lower %*DR* despite the suppression of Reynolds shear stress. (In addition, there is a suppression of the combined slow and rapid contributions to the pressure–strain rate ϕ_{11}^{s+r} and total destruction rate $\epsilon_{11} + \Gamma_{11}$, resulting in an increase in $\langle u^2\rangle$; see Dimitropoulos *et al.* 2001, Ptasinski *et al.* 2003.) In contrast, in HTSF mean shear is fixed so that the monotonic suppression in $-\rho\langle uv\rangle$ produces a monotonic reduction in $\langle u^2\rangle$.

The increase in mean shear in an emerging elastic layer as polymer is added to a channel flow can be understood as a consequence of the suppression of turbulent momentum flux to the surface. In figure 5 we compare the polymer state to the initial Newtonian state before the polymer is added. In a channel flow experiment, this is equivalent to maintaining fixed pressure drop, wall shear stress and u_τ with increasing polymer concentration and measuring %*DR* as a relative increase in flow rate. In this situation, the total flux of momentum to the wall is fixed as the polymer is added. Thus, as turbulent flux is suppressed by polymer–turbulence interactions in the high-shear inertia-dominated elastic layer outside the viscous sublayer, total momentum flux (i.e. stress) must be maintained. The increase in polymer stress as

%DR increases is insufficient to maintain the same total stress in the elastic layer (note in figure 5*a* that the sum of Reynolds + polymer stress reduces with increasing %DR in the low-DR regime), so mean viscous stress (i.e. mean shear rate) increases to make up the difference. The elastic layer emerges from the lower margins of the classical log layer as the polymer is introduced. Thus, as with the rest of the surface layer above, the elastic layer is characterized by u_τ and y with higher-than-Newtonian mean shear. The elastic layer therefore emerges with law-of-the-wall scaling for mean velocity gradient and the log law for mean velocity, but with a lower von Kármán constant (Virk 1971*b*, 1975; L'vov *et al.* 2004).

At low %DR, the higher shear in the elastic layer apparently maintains a sufficient increase in production of $\langle u^2\rangle$ in the presence of decreasing $-\rho\langle uv\rangle$ to keep $\langle u^2\rangle$ roughly constant at low DR. However, figure 5(*a*) shows that the transition to high DR is associated with a more rapid reduction in Reynolds stress as well as a drop in $\langle u^2\rangle$, suggesting that the increase in production by higher mean shear in the elastic layer is no longer sufficient to maintain constant $\langle u^2\rangle$. The entire Reynolds stress tensor is therefore suppressed. In HTSF mean shear is fixed, so that the total flux and the production of $\langle u^2\rangle$ decrease monotonically as the polymer effect is increased. We conclude that the maintenance of constant streamwise velocity variance with increasing polymer concentration in the channel flow is an indirect consequence of the polymer suppression of turbulent momentum flux and not a primary mechanism underlying DR.

Although $\langle u^2\rangle$ varies differently with %DR in HTSF versus channel flow when $DR \lesssim 35\%$, $\langle u^2\rangle/q^2$ increases with polymer in both HTSF and channel flow simulations, as shown in figure 6(*a,d*). Also, other components of $\langle u_i u_j\rangle/q^2$ decrease with polymer both in HTSF and channel flow simulations. Comparison of figure 6(*a,d*) also shows that a polymer enhances the anisotropy of the Reynolds stress tensor $\langle u_i u_j\rangle$ in HTSF consistent with the increasing anisotropy and We_S with decreasing y^+ in channel flow simulations; this reflects the highly anisotropic nature of polymer (under shear) itself, as shown in the anisotropy of polymer conformation and stress tensors (figures 6*b,c* and 1). At the end of § 7 we shall show statistically how preferential suppression of pressure–strain rate correlations by polymer leads to this enhancement of anisotropy in the Reynolds stress tensor.

It is important to note that from the channel flow experiments (figure 5*a*), peak $\langle u^2\rangle$ and TKE are strongly suppressed by polymer when %DR exceeds $\sim 35\,\%$. This results when there is sufficient suppression of the production of Reynolds shear stress to suppress the production of TKE. Interestingly, $\langle u^2\rangle$ is observed to decrease at the %DR that has been generally identified by experimentalists as the transition between low- and high-%DR regimes (Warholic *et al.* 1999; Ptasinski *et al.* 2001).

Note that the increase in polymer stress T_{12}^p between the experiments and simulations with %DR are similar. Experimentally, the correlation coefficient ρ_{uv} between streamwise and vertical velocity fluctuations decreases with increasing %DR (figure 5*a*). Figure 5(*b*), by contrast, suggests that in HTSF the streamwise and vertical fluctuations only decorrelate at higher %DR. However, this apparent difference is a consequence of the drop in $\langle u^2\rangle$ in HTSF; if the correlation coefficient in figure 5(*b*) were adjusted for constant $\sqrt{\langle u^2\rangle}$ as in the experiments, it too would exhibit a drop in correlation coefficient. Furthermore, whereas the increase in %DR in figure 5(*b*) is obtained by increasing We_S with β held fixed , in § 6 we shall show that DR also results when concentration parameter $1-\beta$ is increased at fixed We_S. In this case we find that ρ_{uv} decreases with increasing $1-\beta$ when $We_S \gtrsim 3$.

One of the most important and consistently measured consequences of polymer–turbulence interactions is the suppression of turbulent dissipation rate and therefore

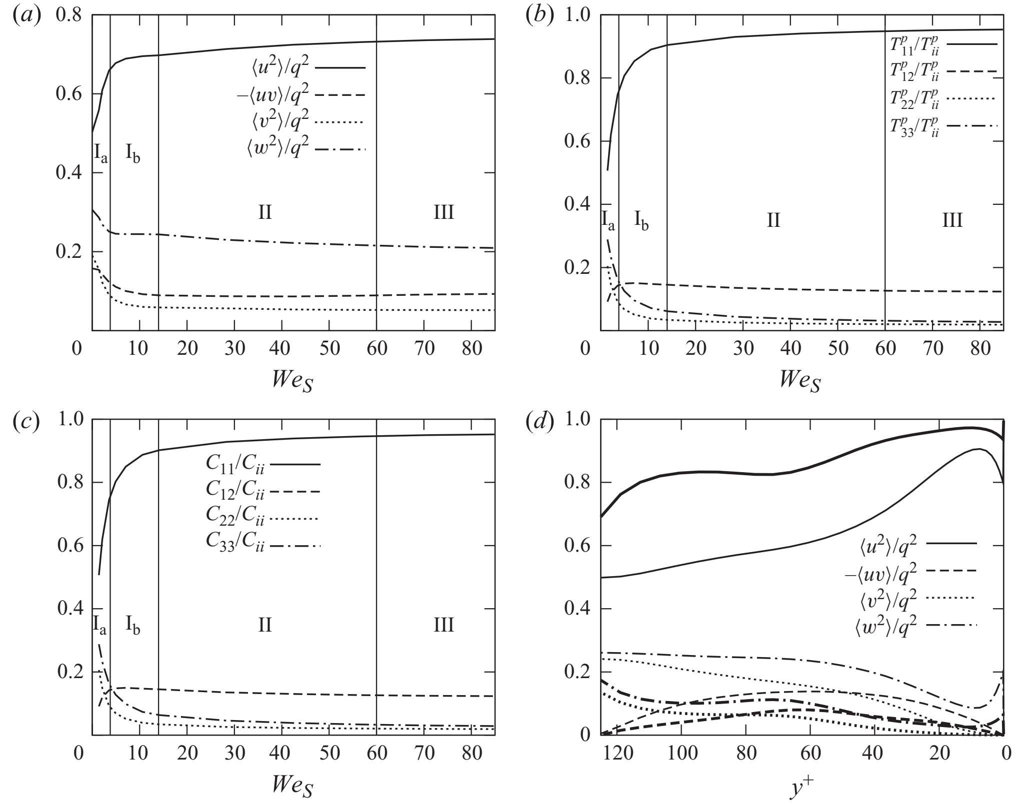

FIGURE 6. Effect of Weissenberg number We_S $(1-\beta=0.05)$ on normalized (*a*) Reynolds stresses $(\langle u_i u_j\rangle/q^2)$, (*b*) polymer stresses (T^p_{ij}/T^p_{ii}) and (*c*) conformation tensor (C_{ij}/C_{ii}) in HTSF. (*d*) $\langle u_i u_j\rangle/q^2$ versus y^+ from channel flow simulations. Thick and thin lines are for polymer $(DR=30\,\%)$ and Newtonian simulations, respectively. Figure 1 shows how We_S increases towards the wall. Channel flow data used are from Housiadas & Beris (2003, 2005). The regimes I–III are defined and discussed in context with figure 8.

small-scale turbulence fluctuations. As previously discussed, the HTSF DNS produces a dramatic suppression of the dissipation rate (figure 3*f*). In figure 7 we compare predicted and experimental one-dimensional streamwise velocity spectra as a function of $\%DR$. The experimental spectra were measured by Warholic *et al.* well above the viscous wall layer. In both HTSF simulations and experiments, turbulent energy is suppressed at the smallest scales by the addition of a polymer. At higher $\%DR$, in particular, turbulent energy is strongly suppressed primarily at the smallest scales consistent with the HTSF simulations. In addition, at high $\%DR$ the spectra approach similar fixed points in both the experiments and HTSF simulations. In the experiments, this fixed point is the MDR limit. As we shall discuss in the next section, HTSF simulations also approach an MDR-like asymptotic state at high Weissenberg numbers.

The comparisons made in this section are a strong support for the claim that HTSF with the FENE-P model captures the fundamental statistical behaviour of polymer DR in wall-bounded shear flows with drag reducing polymer additive. In the following, we analyse our HTSF simulations statistically to further explore basic mechanisms underlying polymer DR.

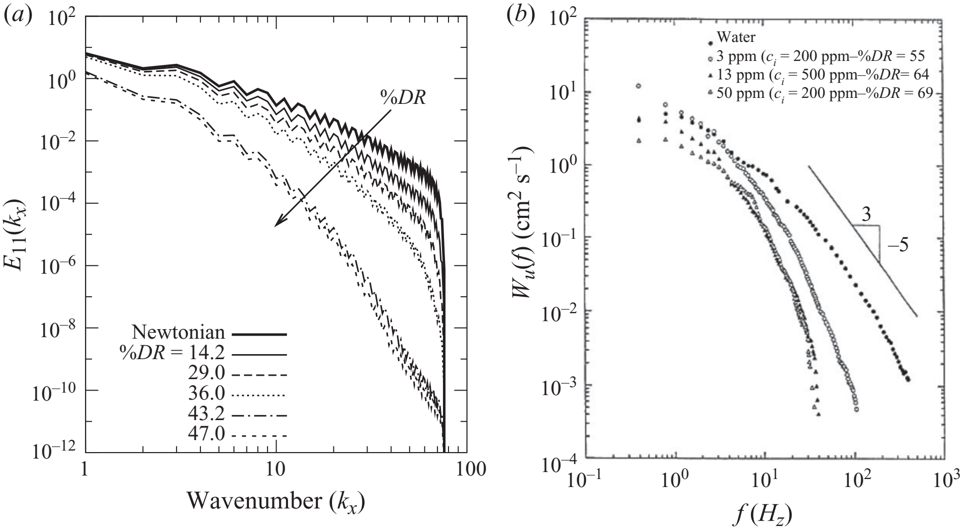

FIGURE 7. Effect of polymer addition on one-dimensional streamwise velocity spectra, shown as a function of %*DR* (*a*) from 256^3 HTSF simulations (256A, B, D, K, M) and (*b*) from the channel flow experiments of Warholic *et al.* (1999) at $y/H = 0.3$, where H is the half-channel width. Refer to table 1 for interpretation of the letters and details of the simulations.

6. Drag reduction regimes: turbulent versus polymer momentum flux

At fixed flow rates, polymer DR implies the reduction of surface shear stress with the addition of a polymer and a reduction in total momentum flux to the surface. In the elastic layer, the total flux of momentum to the surface is given by the sum of Reynolds shear stress and polymer shear stress, $-\rho\langle uv\rangle + T^p_{12}$. The experimental channel flow results of figure 5(*a*) show a monotonic decrease in $-\rho\langle uv\rangle + T^p_{12}$ with increasing %*DR*.

In figure 8(*a,b*) we plot the change in Reynolds shear stress $-\rho\langle uv\rangle$, polymer shear stress T^p_{12} and total stress $T_{tot} = -\rho\langle uv\rangle + T^p_{12}$, as functions of increasing Weissenberg number We_S (left axis) and %*DR* (right axis) calculated from (5.1) from the polymer-laden homogeneous shear flow simulations at fixed polymer concentration parameter $1-\beta = 0.05$. First consider the change in %*DR* up to $We_S = 14$, regime I in figure 8(*b*), mirrored by a corresponding but opposite change in total stress, $-\rho\langle uv\rangle + T^p_{12}$. As polymer effect is increased from the Newtonian state, the %*DR* initially increases rapidly with increasing We_S to a temporary plateau when $We_S \gtrsim 7$ (after a temporary peak). Figure 8(*a*) shows that when $We_S \approx 14$, %*DR* begins another much more gradual increase, through regime II, before asymptoting to a relatively fixed %*DR* above $We_S \approx 60$ in regime III. In this asymptotic state, further increases in polymer effect produce no further increases in DR similar to the MDR limit observed in experiments of polymer-laden internal flows (Virk 1975; Warholic *et al.* 1999; Ptasinski *et al.* 2001). Similarly to experiments, figure 8(*a*) indicates that this asymptotic MDR state is characterized by a severe suppression of the turbulent momentum flux $-\rho\langle uv\rangle$ and the dominance of polymer stress T^p_{12}.

The low-DR regime I in figure 8(*b*) is characterized by a rapid growth in %*DR* with We_S to a plateau. This regime is marked by rapid growth in polymer stress T^p_{12} from zero in the Newtonian state concurrent with a rapid drop in Reynolds stress $-\rho\langle uv\rangle$ from its Newtonian value. The drop in $-\rho\langle uv\rangle$ is so rapid that it

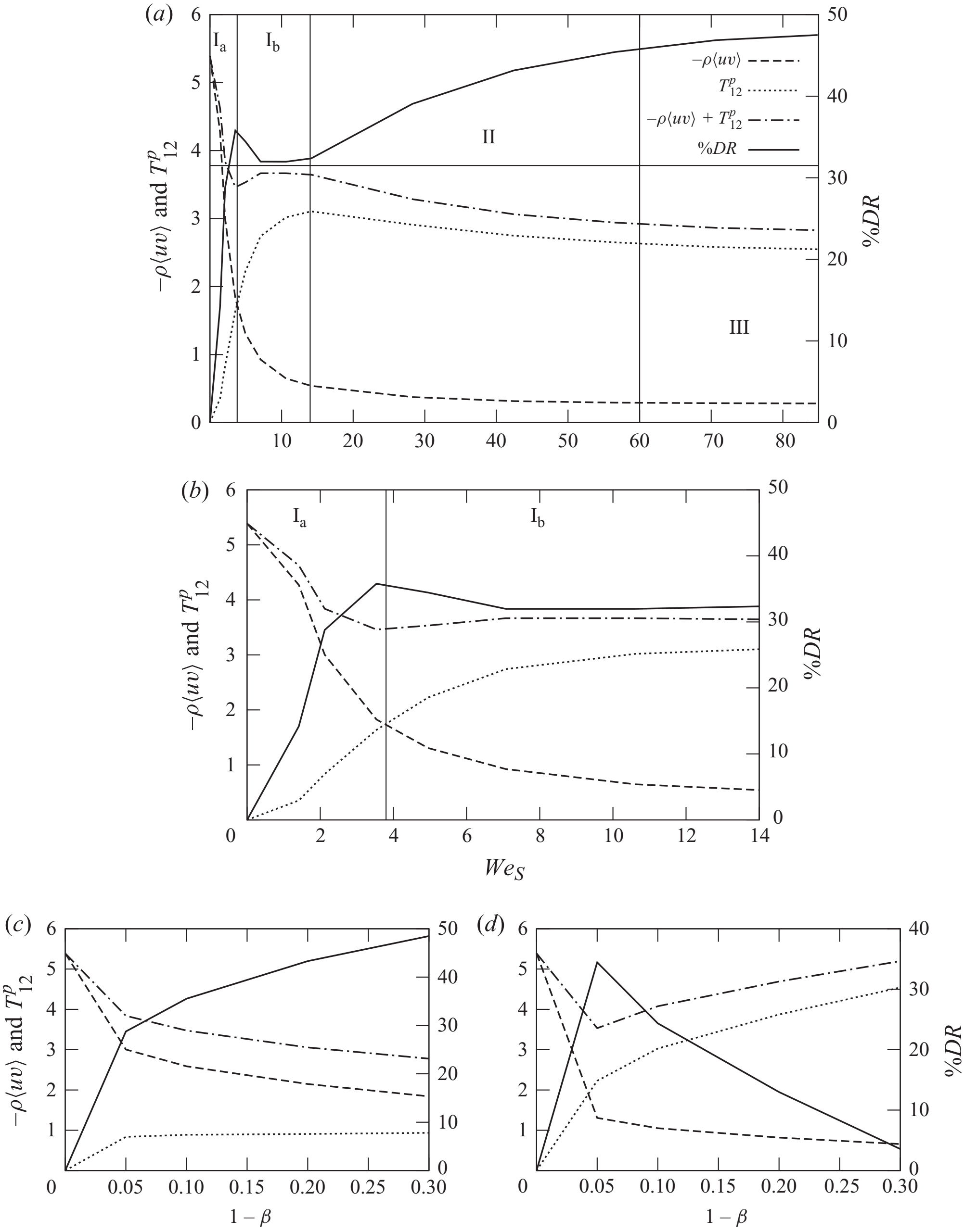

FIGURE 8. Variation in Reynolds stress $-\rho\langle uv\rangle$, mean polymer stress T^p_{12}, total stress $-\rho\langle uv\rangle + T^p_{12}$ and $\%DR$ calculated from (5.1) with (*a*, *b*) Weissenberg number We_S at fixed $1-\beta=0.05$ and (*c*, *d*) with polymer concentration parameter $1-\beta$ at fixed Weissenberg numbers, where in (*c*) $We_S=2.1$ and in (*d*) $We_S=5.0$. (*b*) expands (*a*) up to $We_S=14$ to show regions $\mathrm{I_a}$ and $\mathrm{I_b}$ more clearly.

overwhelms the increase in T^p_{12} and forces a drop in total stress $-\rho\langle uv\rangle + T^p_{12}$, with a corresponding increase in $\%DR$. The Weissenberg number where Reynolds stress and polymer stress cross is an anomalous point at which the total stress is locally a minimum and $\%DR$ momentarily peaks; this anomaly may reflect the fact that mean shear is fixed in HTSF while mean shear increases in the elastic layer with the addition of a polymer to the boundary layer. The main point is that regime I is characterized by a rapid increase in $\%DR$ to a temporary plateau at roughly 30 % DR with characteristics qualitatively similar to the low-DR regime in polymer-laden channel flow (figure 5*a*). A similar rapid increase and plateau is observed in figure 6 for anisotropies of Reynolds and polymer stresses.

We further divide regime I in figure 8(*a*,*b*) into regimes $\mathrm{I_a}$ and $\mathrm{I_b}$, where the separation between the two regimes is the point of crossover in dominance between the polymer and Reynolds shear stresses. More importantly, regime $\mathrm{I_a}$ is distinguished by extreme sensitivity to increases in polymer effect. This high sensitivity is apparent both with increases in We_S at fixed concentration (figure 8*b*) and with increases in concentration parameter $1-\beta$ at fixed Weissenberg number (figure 8*c*,*d*). The sensitivity in the low-DR regime $\mathrm{I_a}$ quickly diminishes into regime $\mathrm{I_b}$ as the $\%DR$ plateaus and polymer stress T^p_{12} maximizes at $We_S \approx 14$. $\mathrm{I_b}$ can also be considered a regime in which polymer stress transitions to dominate Reynolds shear stress.

The peak in T^p_{12} demarcates the transition to a high-DR regime II marked by much less sensitivity to changes in the polymer relaxation time We_S, and a gradual reduction in both polymer stress and Reynolds stress, contributing to increasing $\%DR$ with polymer effect. In regime II polymer stress strongly dominates Reynolds shear stress. Reynolds and polymer anisotropies move gradually towards an asymptotic value (figure 6).

Figure 8(*c*,*d*) shows the corresponding changes in Reynolds stress, polymer stress and total stress with increasing concentration parameter, $1-\beta$. Figure 8(*c*) shows predictions for lower values of We_S, in regime $\mathrm{I_a}$, while We_S is higher in figure 8(*d*), in regime $\mathrm{I_b}$. Although $\%DR$ increases continuously with increasing $1-\beta$ at the lower We_S similarly to figure 8(*a*), at the higher We_S the simulations predict a peak in $\%DR$ followed by a continuous decrease at high $1-\beta$. The peak is a reflection of a more rapid increase in polymer stress relative to the drop in Reynolds stress than is the case in figure 8(*a*–*c*). Interestingly, there is some experimental evidence of the possible existence of a peak in $\%DR$ with increasing concentration. Wu (1969) and Wu & Tulin (1972) report data consistently showing the existence of peaks in $\%DR$ with dilute homogeneous mixtures of Polyox WSR-301 over both smooth and rough flat plates. They compare their results to other data in the literature with similar peaks and indicate that the peak in $\%DR$ is more prevalent with uniform mixtures of polymer than with injected polymer.

The main result from figure 8 is that the homogeneous turbulent flow with polymer and shear has remarkably similar behaviour to polymer-induced DR in channel and pipe flows. Similarly to experiments, the high-DR regime is marked by a transition in which the entire Reynolds shear tensor is suppressed, including Reynolds shear stress and component variances (figure 5). At high DR, the severe suppression of TKE by polymer–turbulence interactions causes the mean gradient production terms to play a dominant role in the polymer energy budget and Newtonian transport of momentum is replaced by a non-classical mechanism associated with fluctuations in polymer stretch and stress. In addition, figure 3(*c*,*f*) shows that turbulence dissipation rate is severely suppressed by polymer–turbulence interactions, even within the low-DR regime, consistent with the predicted and experimentally observed suppression of small-scale strain rate fluctuations (figure 7). In both experiments and simulations, the MDR state is an asymptotic limit of the high-DR regime in which turbulence production is not entirely suppressed, but is rather maintained by polymer–turbulence interactions.

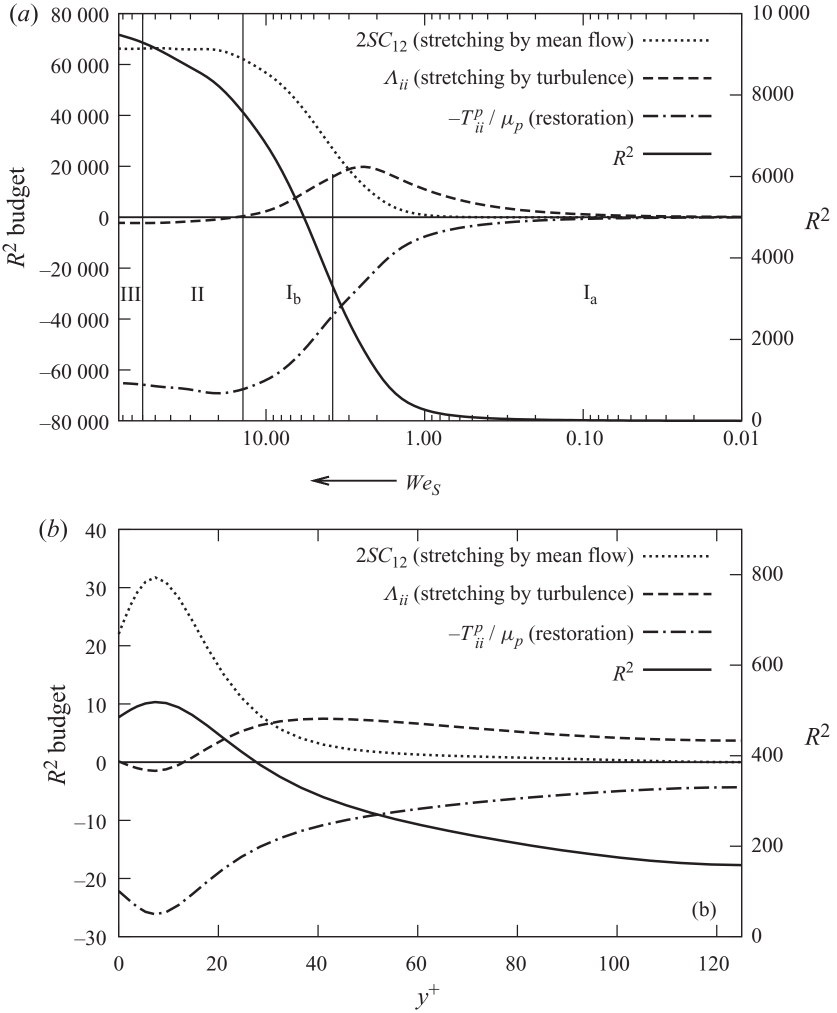

FIGURE 9. (*a*) Change in the mean polymer stretch R^2 (right axis) and the terms (left axis) in the budget for R^2 (see (2.19)) with increasing Weissenberg number in HTSF and (*b*) with increasing y^+ in channel flow with $DR = 30\,\%$. We_S increases as the wall is approached ($y^+ = 0$) as shown in figure 1. Channel flow data used are from Housiadas & Beris (2003, 2005).

In figure 9(*a*) we plot the terms in the budget for mean polymer stretch R^2 (see (2.19)). Note that We_S increases from right to left on a log scale as compared with figure 9(*b*). The polymer is stretched by mean shear ($2SC_{12}$) and by fluctuating strain rate (Λ_{ii}), and the restoration term ($-T^p_{ii}/\mu_p$) maintains finite polymer length. We have identified in figure 9(*a*) the characteristics of the polymer stretch balance that are associated with the different DR regimes of figure 8(*a*). In the low-DR regime $\mathrm{I_a}$, the stretching of polymer by fluctuating strain rate dominates the stretching by mean shear. As We_S increases, strain rate fluctuations are progressively suppressed, Λ_{ii} is correspondingly reduced and the stretching of the polymer by mean shear increases. Thus, regime $\mathrm{I_b}$ is characterized by a transition to a state where the stretching of the polymer by mean shear dominates stretching by turbulent strain rate fluctuations. In the high-DR regime II and the asymptotic MDR regime III, polymer stretching R^2

is fully dominated by mean shear. In fact, stretching of the polymer by fluctuating strain rate is slightly negative in regimes II and III.

In figure 9(*b*) we make an interesting comparison with the channel flow simulation of Housiadas & Beris (2003, 2005). As shown in figure 1, We_S increases with decreasing y^+; the increase is particularly rapid through the elastic layer ($y^+ \approx 10$–50 in figure 1). In figure 9(*a*) we plotted the We_S axis with a log scale and in reverse direction to compare better with the channel flow data in figure 9(*b*). Note the great similarity in the qualitative trends in the R^2 budget between the channel and homogeneous shear flow simulations. In particular, note how in the channel flow the turbulent stretching term Λ_{ii} initially increases with increasing We_S, reaches a peak and then decreases and goes negative at the highest We_S close to the wall. The same behaviour is observed in figure 9(*a*) with increasing We_S in HTSF. Similarly, mean stretching $2SC_{12}$ and restoration $-T_{ii}^{p}/\mu_p$ peak close to the wall and become comparable in channel flow with the same trends at high We_S in HTSF. The primary difference between the two flows is the existence of a viscous layer in channel flow where turbulence variables are forced to zero at the wall. This further supports our conclusion that HTSF models the essential drag reducing mechanisms in the inertia-dominated regions of the channel flow.

The comparisons and discussions in §§ 5 and 6 validate the argument that the essential mechanisms underlying DR are contained within the polymer–turbulence interactions found in HTSF. The following two sections further describe the analysis of the HTSF simulations to quantify essential statistical characteristics of DR from initiation and through the low-, high- and asymptotic-DR regimes when polymer–turbulence interactions are in equilibrium.

7. The statistics of Reynolds stress suppression, the central role of pressure–strain rate inter-component energy transfer and the MDR limit

The suppression of momentum flux through the lower inertial wall layer by polymer–turbulence interactions requires the suppression of the Reynolds shear stress, and therefore redistributions of TKE and restructuring of the Reynolds stress tensor. Here we describe this restructuring and the underlying changes in the Reynolds stress budgets that lead to its restructuring. It will be useful for the reader to review the budget equations (2.7)–(2.10) for HTSF with the related equations for polymer–turbulence energy exchange $\Gamma_{\alpha\beta}$, (2.13), and the three contributions to pressure–strain rate inter-component energy transfer $\phi_{\alpha\beta}$ from slow, rapid and polymer contributions to fluctuating pressure, (2.11).

Since the production of $-\langle uv\rangle$ is proportional to the vertical velocity variance $\langle v^2\rangle$ and mean shear (see (2.10)), it is not surprising to observe in figure 10 that $\langle v^2\rangle$ is the first component of the Reynolds stress tensor to respond to the presence of polymer in the shear flow. What is perhaps surprising is the sensitivity with which $\langle v^2\rangle$ is suppressed by polymer even at the lowest Weissenberg numbers: the reduction of $\langle v^2\rangle$ with increasing polymer effect significantly precedes the suppression of all other Reynolds stress components. The suppression of $\langle v^2\rangle$ by polymer–turbulence interactions causes a suppression of Reynolds shear stress and because $-\langle uv\rangle$ is in the source term to $\langle u^2\rangle$, the suppression of vertical velocity variance follows the suppression of $-\langle uv\rangle$ at a significantly later time. The suppression of spanwise velocity variance $\langle w^2\rangle$ occurs at about the same time as $\langle uv\rangle$.

The budgets for $\langle v^2\rangle$ and $\langle w^2\rangle$ in Newtonian fluids contain no source terms (see (2.8) and (2.9)). Unlike $\langle u^2\rangle$, which receives energy from the interaction between mean shear and Reynolds shear stress, the only statistical mechanism to maintain vertical and

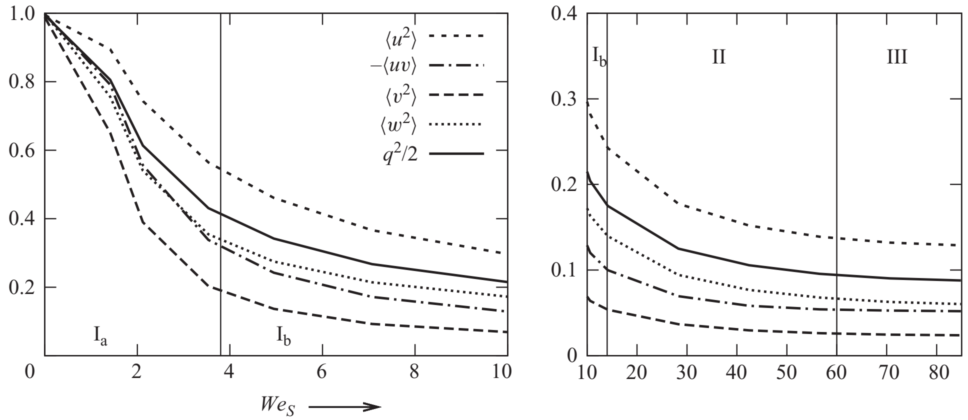

FIGURE 10. The suppression of the Reynolds stress components $\langle u_i u_j\rangle$ relative to their Newtonian values ($\langle u_i u_j\rangle_{polymer}/\langle u_i u_j\rangle_{Newtonian}$) with increasing Weissenberg number We_S.

spanwise fluctuations is the transfer of energy from $\langle u^2\rangle$ via correlations between fluctuating pressure and strain rate fluctuations. In the presence of polymer, however, polymer–turbulence interactions can, in principle, transfer energy from polymer elastic energy to $\langle v^2\rangle$ and $\langle w^2\rangle$ through the $\Gamma_{\alpha\alpha}$ terms in (2.8) and (2.9). Figure 11 shows the influence of polymer on the budgets of the Reynolds stress components in the order in which they are suppressed by polymer from figure 10. We observe that the polymer–turbulence interactions terms are always sinks in the evolution of all Reynolds stress components. Thus, even in the presence of polymer, vertical and spanwise turbulence fluctuations maintain variance only through the pressure–strain correlation terms $\phi^t_{\alpha\alpha}$; the total pressure–strain removes streamwise velocity variance and delivers it to $\langle v^2\rangle$ and $\langle w^2\rangle$.

7.1. *Drag reduction with low polymer effect*

The process of DR initiates with the suppression of vertical velocity variance as a consequence of polymer–turbulence interactions. Figure 11(*a*) shows that, in the equilibrium state, incipient polymer effect is associated with a strong suppression of component dissipation rate (i.e. strain rate fluctuations) as a new dissipative mechanism, polymer–turbulence energy exchange (Γ_{22}), grows. Net dissipation rate, however, remains roughly independent of the Weissenberg number until it is suppressed overall as We_S increases to move the state of the turbulent shear flow from regime I$_a$ to I$_b$ and then into the high-DR regime II. The growth of Γ_{22} is a reflection of the stretching of polymer by turbulence strain rate fluctuations ($\Lambda_{\alpha\alpha}$, figure 9, (2.19)) which, itself, reduces the level of strain rate fluctuations while maintaining a fixed total rate of destruction. At slightly higher We_S, the suppression of vertical velocity variance and strain rate fluctuations becomes so severe that the turbulence can no longer maintain the same level of polymer stretch as before, so Γ_{22} and total destruction rate decrease as the system transitions from regime I$_a$ to I$_b$. A similar process takes place with the $\langle w^2\rangle$ budget, and also with $\langle u^2\rangle$, albeit with somewhat weaker influence.

The more important observation from figure 11 is that, as the level of polymer in the shear flow increases and the state of the shear flow moves from regime I$_a$ to regime I$_b$, and then into regime II, the only statistical mechanism that can account for the strong

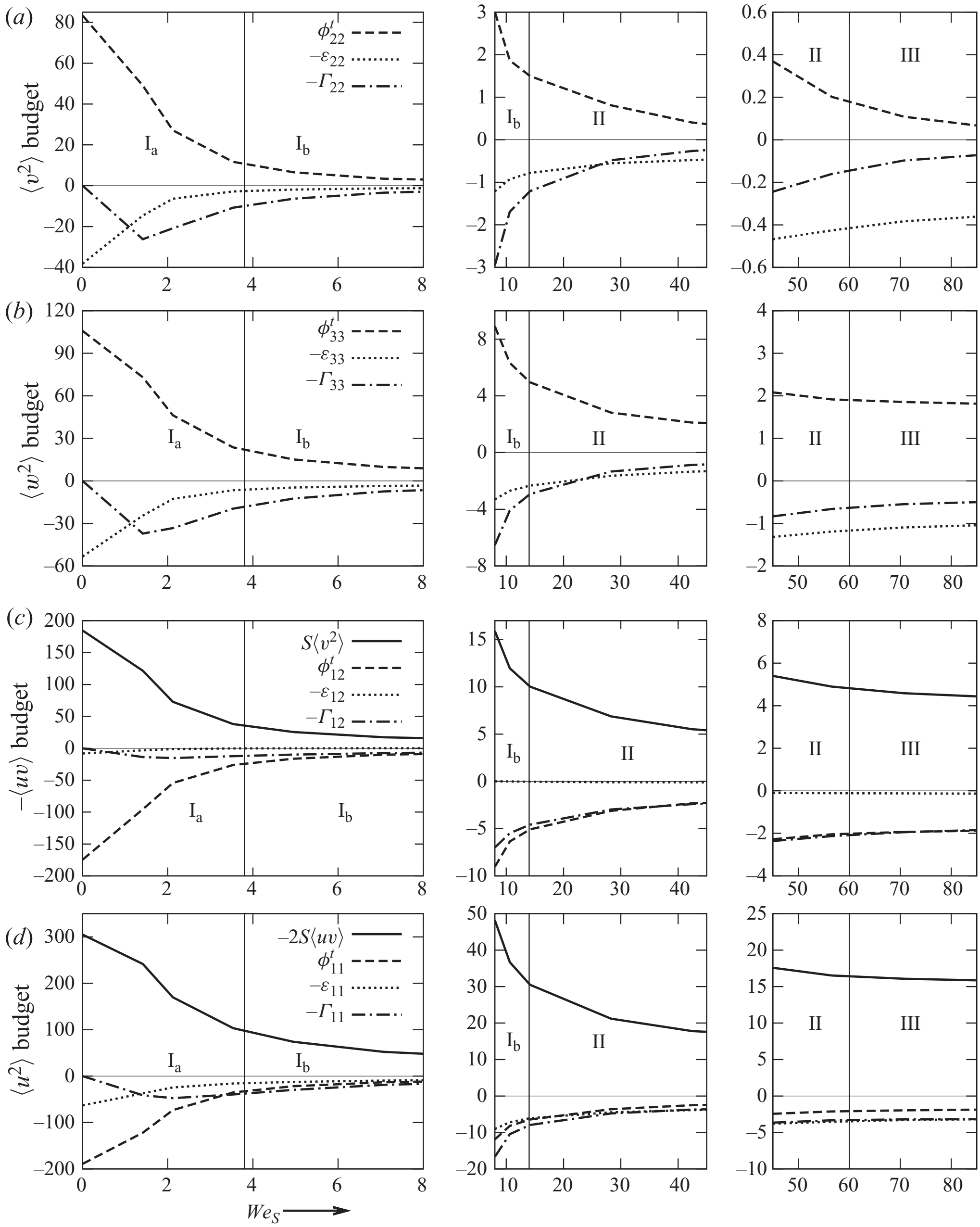

FIGURE 11. Change in the terms in the budget for (*a*) vertical velocity variance, $\langle v^2 \rangle$ (see (2.8)), (*b*) spanwise velocity variance, $\langle w^2 \rangle$ (see (2.9)), (*c*) Reynolds shear stress, $-\langle uv \rangle$ (see (2.10)) and (*d*) streamwise velocity variance, $\langle u^2 \rangle$ (see (2.7)) with increasing Weissenberg number.

suppression of vertical velocity variance is a strong suppression of the pressure–strain rate correlation as a consequence of polymer–turbulence interactions. Comparing the suppression of pressure–strain rate energy transfer ϕ^t_{22} into $\langle v^2 \rangle$ in figure 11(*a*) with corresponding reductions in $\phi^t_{\alpha\alpha}$ in the other components suggests that the suppression of ϕ^t_{22} with increasing Weissenberg number is significantly stronger than the other components. This particular sensitivity of ϕ^t_{22} to the presence of polymer is responsible for the initial suppression of vertical velocity variance that sets off the cascade of suppressions that lead to Reynolds shear stress and TKE suppression, and DR.

7.2. *Drag reduction with high polymer effect and the MDR asymptotic limit*

In the Newtonian state, Reynolds shear stress is maintained by a balance between production, proportional to $\langle v^2\rangle$, and destruction by pressure–strain rate correlations (figure 11*c*). However, as the polymer is added and the Weissenberg number increases, destruction of Reynolds shear stress by polymer stretch (Γ_{12}) grows until, in the high-DR regime, it contributes as much to Reynolds stress destruction as does friction. The budget of $\langle u^2\rangle$ (figure 11*d*) shows that the production of $\langle u^2\rangle$ ($-2S\langle uv\rangle$) decreases with the suppression of Reynolds shear stress. Similarly to the $-\langle uv\rangle$ budget, the rate of energy transfer from $\langle u^2\rangle$ into polymer elastic energy (Γ_{11}) grows into regime II where it becomes a stronger destructive mechanism than pressure–strain rate (ϕ^t_{11}). The strong suppression of ϕ^t_{11} by polymer–turbulence interactions is important to the redistribution of variance within the Reynolds stress tensor since the rate of inter-component energy transfer from $\langle u^2\rangle$ to $\langle v^2\rangle$ and $\langle w^2\rangle$ is correspondingly reduced.

The observation that the suppression of $\langle v^2\rangle$ by polymer–turbulence interactions initiates the suppression of $-\langle uv\rangle$ (and therefore DR) and leads to the suppression of $\langle u^2\rangle$ has, at its core, the suppression of pressure–strain rate inter-component energy transfer is consistent with similar conclusions reached by Walker & Tiederman (1990), Dimitropoulos *et al.* (2001) and Ptasinski *et al.* (2003). What is particularly interesting is the influence of the polymer on the relationships among the contributions to pressure–strain rate correlations, shown in figure 12, which shows that the Newtonian balance between rapid and slow pressure–strain rate is severely altered by the presence of polymer while the direct role of polymer pressure–strain rate itself is important only in the asymptotic MDR limit. In the Newtonian state, energy is transferred from $\langle u^2\rangle$ equally within the rapid and slow pressure–strain rate terms. However, $\langle v^2\rangle$ receives energy from the slow part while $\langle w^2\rangle$ receives energy primarily from the rapid part.

Polymer–turbulence interactions dramatically suppress all pressure–strain rate contributions as polymer effect (i.e. We_S) increases through the low-DR regime I. This suppression is particularly strong in the slow pressure–strain rate transfer of energy to $\langle v^2\rangle$, with the effect that energy transfer to vertical velocity fluctuations is severely blocked. As polymer effect increases with increasing Weissenberg number and the turbulent HTSF moves into the high- and asymptotic-DR regimes II and III, the removal of energy from $\langle u^2\rangle$ by the slow pressure–strain rate contribution ϕ^s_{11} is nearly entirely suppressed and the rapid term ϕ^r_{11} takes over as the primary inter-component energy transfer mechanism removing energy from $\langle u^2\rangle$. However, in the MDR limit (regime III), the rapid term transfers energy into the spanwise fluctuations rather than vertical fluctuations. The vertical velocity variance $\langle v^2\rangle$ receives what little energy can be transferred from $\langle u^2\rangle$ through the slow term ϕ^s_{22} and supplements it with energy from $\langle w^2\rangle$ through the rapid term ϕ^r_{22}.

Figure 12(*c*) shows that without the polymer contribution to the inter-component energy transfer through pressure–strain rate correlation in the MDR limit, the vertical fluctuations would lose energy through rapid pressure–strain rate and dissipation, so that eventually $\langle v^2\rangle$ would die out completely, production of Reynolds stress and $\langle u^2\rangle$ would cease, and the flow would re-laminarize. In the MDR limit, the normal Newtonian mechanism that keeps turbulence alive is suppressed, and replaced with a dynamics in which the transfer of energy to vertical fluctuations by polymer–turbulence interactions through pressure–strain rate correlations plays an essential

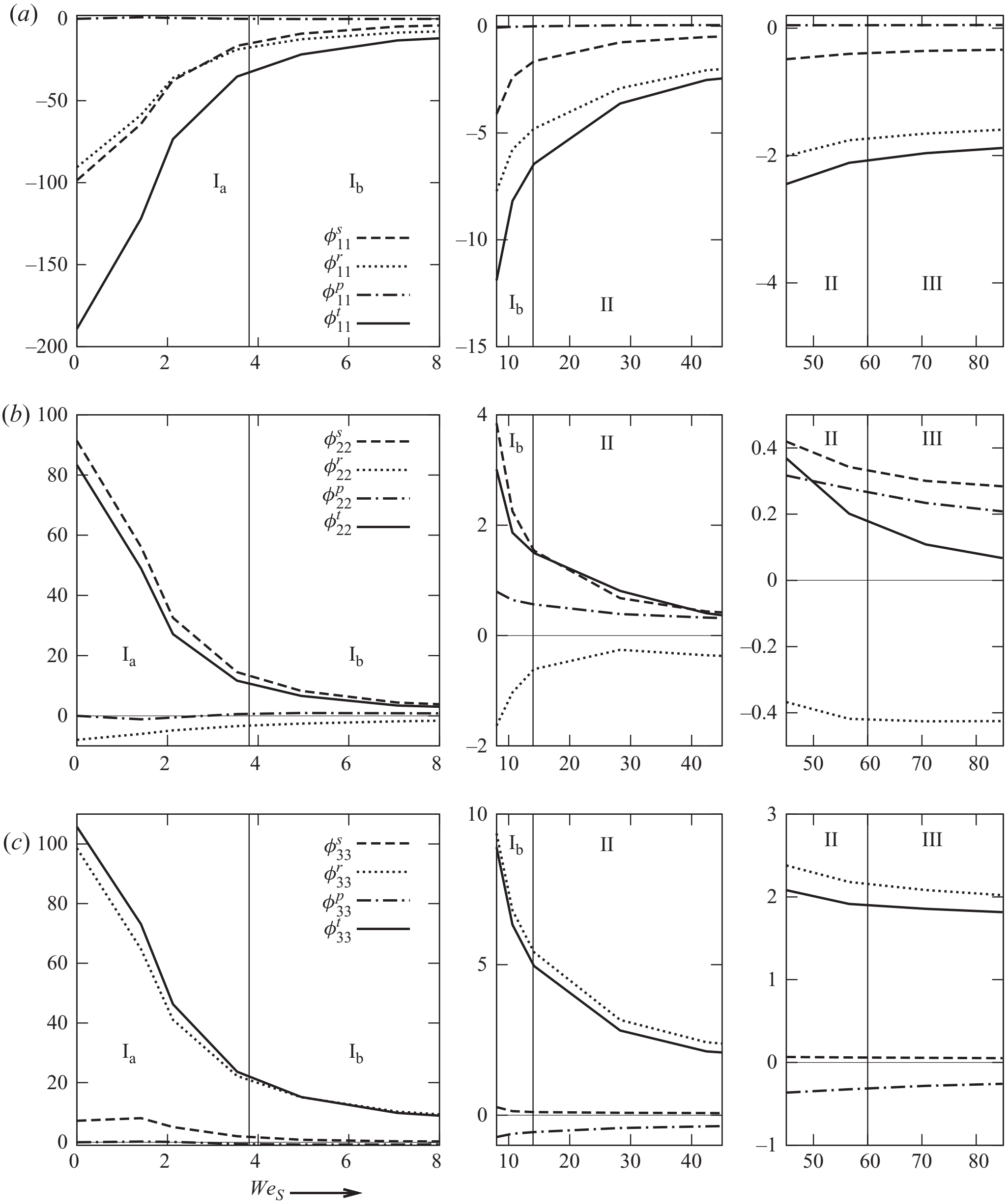

FIGURE 12. Change in the pressure–strain rate inter-component energy transfer components (*a*) 11, (*b*) 22 and (*c*) 33 with increasing Weissenberg number.

role in the maintenance of the turbulent state. At MDR, polymer DR hinges on the maintenance of $\langle v^2 \rangle$ through polymer pressure–strain rate transfer of component kinetic energy into $\langle v^2 \rangle$.

The polymer contribution to the inter-component energy transfer through pressure–strain rate correlation is, from figure 12, not significant until the MDR limit. In figure 13 we isolate the polymer contribution to inter-component energy transfer. A dramatic change in the structure of the polymer pressure–strain rate correlations

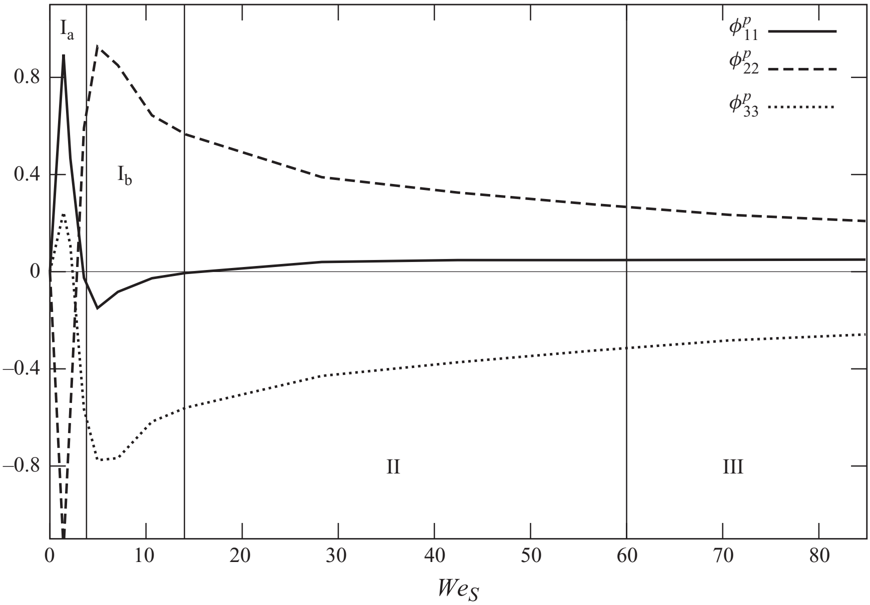

FIGURE 13. In the asymptotic limit of high We_S turbulence is maintained by the polymer pressure–strain rate contribution ϕ^p_{22} where polymer transfers energy into $\langle v^2 \rangle$ ($\phi^p_{22} > 0$) from $\langle w^2 \rangle$ ($\phi^p_{33} < 0$).

occurs during the incipient addition of the polymer at low We_S. As polymer effect increases and the state of the system moves from $\mathrm{I_a}$ to $\mathrm{I_b}$ in the low-DR regime, all the polymer pressure–strain rate components change sign, and in the asymptotic MDR limit, when the polymer pressure–strain rate plays the critical role of keeping $\langle v^2 \rangle$ alive, energy moves into $\langle v^2 \rangle$ from $\langle w^2 \rangle$ – a very different process from the Newtonian shear flow where energy moves into $\langle v^2 \rangle$ from $\langle u^2 \rangle$.

These results indicate that while it is in the direct suppression of $\langle v^2 \rangle$ that polymer–turbulence interactions lead to DR, in the MDR limit turbulence is kept alive by inter-component transfer of energy to $\langle v^2 \rangle$ from $\langle w^2 \rangle$ through correlations between the part of the pressure fluctuations created by polymer stress (see (2.11)) and fluctuating strain rate. At the same time, $\langle w^2 \rangle$ maintains its energy through rapid pressure–strain rate correlations that move energy from $\langle u^2 \rangle$ to $\langle w^2 \rangle$. This symbiotic relationship between the Newtonian and polymer contributions to pressure–strain rate is necessary to maintain $\langle v^2 \rangle$ and prevent re-laminarization at the highest levels of polymer effect. Note from figure 9 that the distinguishing characteristic of the high-DR and MDR regimes II and III is that polymer stretch, and therefore polymer stress, is maintained by mean shear rather than turbulent strain rate fluctuations. Thus, both the polymer pressure–strain rate component ϕ^p_{22} that transfers energy to $\langle v^2 \rangle$ and the rapid pressure–strain rate component ϕ^r_{33} that maintains $\langle w^2 \rangle$ variance that is ultimately transferred to $\langle v^2 \rangle$ originate in the interactions between mean shear, polymer stretch and turbulence velocity fluctuations.

These results suggest that the asymptotic limit that is MDR is a delicate balance in which vertical velocity fluctuations are maintained at a low level by mean shear acting on both polymer molecules and turbulence, by mean shear acting on the low-level vertical velocity fluctuations to maintain a low level of Reynolds shear stress (figure 11*c*), and by the low-level Reynolds shear stress being distorted by mean

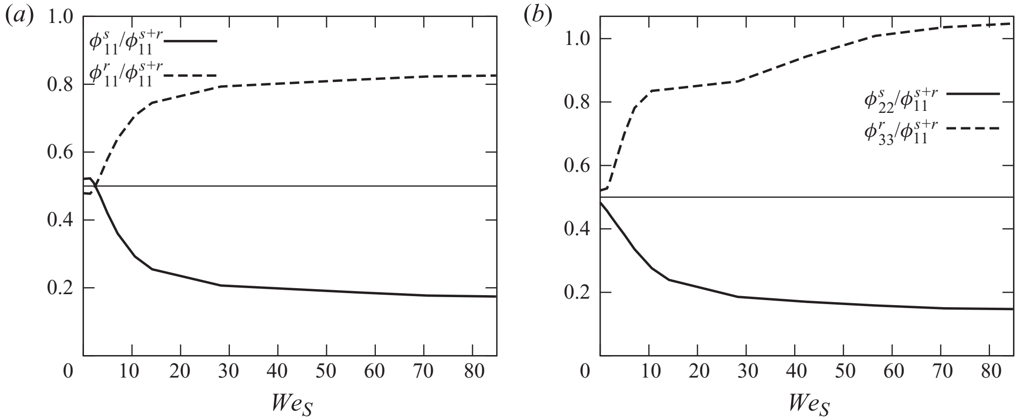

FIGURE 14. (a) Fractions of slow ($\phi^s_{11}/(\phi^s_{11}+\phi^r_{11})$) and rapid ($\phi^r_{11}/(\phi^s_{11}+\phi^r_{11})$) pressure–strain rates inter-component energy transfer available from $\langle u^2\rangle$ with increasing Weissenberg number We_S. (b) Fraction of total inter-component energy received by $\langle w^2\rangle$ through rapid pressure–strain rate ($\phi^r_{33}/(\phi^s_{11}+\phi^r_{11})$) and by $\langle v^2\rangle$ through slow pressure–strain rate ($\phi^s_{22}/(\phi^s_{11}+\phi^r_{11})$) from $\langle u^2\rangle$ with increasing Weissenberg number We_S.

shear to maintain $\langle u^2\rangle$ (figure 11d) which, through rapid pressure–strain rate also keeps $\langle w^2\rangle$ alive. Figure 14 shows that the dramatic enhancement of anisotropy in the Reynolds stress tensor with strong polymer effect arises from the change in balance between slow and rapid pressure–strain rate that arises from polymer–turbulence interactions: the contribution of slow interactions is dramatically suppressed relative to rapid contributions as the polymer shear turbulence moves into the high-DR and MDR regimes. The polymer–turbulence interactions block the Newtonian transfer of energy to vertical velocity fluctuations while creating a new route of energy transfer to $\langle v^2\rangle$ that requires polymer, turbulence and mean shear.

This balance in the high-polymer-effect MDR limit is very different from the low-polymer-effect regime I, where the dynamics of polymer–turbulence interactions centres on the stretching of polymer by fluctuating strain rate and subsequent destruction of fluctuating strain rate in a process that leads to the suppression of vertical velocity fluctuations, Reynolds shear stress and, ultimately, TKE.

8. Polymer effects on turbulence and elastic energy dynamics: homogeneous shear versus channel flow

We have shown that at higher Weissenberg numbers, polymer–turbulence interactions dramatically alter the dynamics of turbulence energy exchange and introduce a new turbulence–polymer energy transfer mechanism. In this section, we address the energy transfer balance in the turbulence–polymer interaction process.

Consider in figure 15 the changes in relative magnitudes of the terms in the kinetic energy budget equation (2.14) with increasing Weissenberg number. All terms in the budget, including the TKE $q^2/2$, asymptote to constant values in the MDR regime III. With fixed mean shear rate, polymer-induced suppression of Reynolds shear stress forces a reduction in TKE (see (2.14)). As discussed in the previous section, viscous dissipation rate (ϵ) is augmented by the transfer of TKE from turbulence to polymer as the polymer is stretched (Γ) in such a way that the total destruction ($\epsilon+\Gamma$)

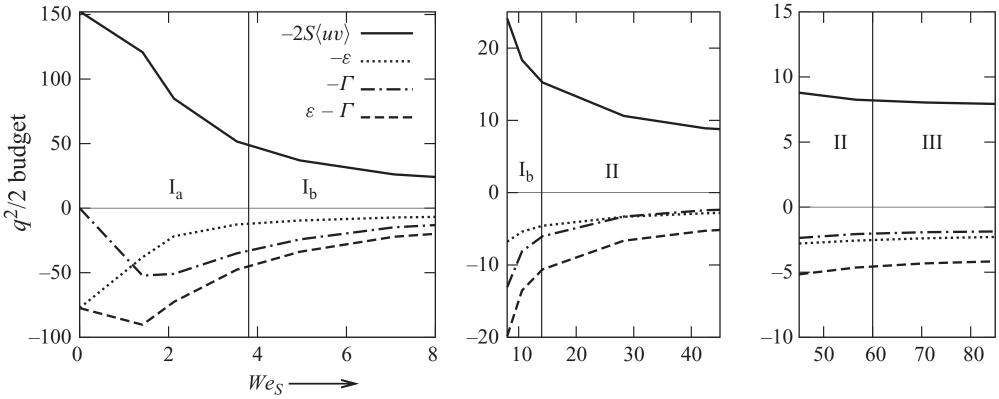

FIGURE 15. Change in the terms in the budget for TKE, $q^2/2$ (see (2.14)), with increasing Weissenberg number.

is roughly independent of increasing Weissenberg numbers at incipient polymer effect. Similarly to component variances (figure 11), at slightly higher We_S where the turbulence transitions through regime $\mathrm{I_b}$ and into the high-DR regime II, viscous, polymer and total TKE destruction are suppressed by the reduction in strain rate fluctuations and TKE overall. In effect, the influence of polymer on turbulence is itself suppressed once the turbulent strain rate fluctuations have done sufficient work on polymer to allow the polymer to interfere with turbulent momentum flux and the Reynolds stress budget. This process is represented by the transition from the incipient DR regime $\mathrm{I_a}$, where strain rate fluctuations are strongly suppressed as they stretch the low levels of polymer to regime $\mathrm{I_b}$, into the high-DR regime II, where fluctuating strain rate and TKE have been sufficiently reduced, so that the interference of polymer in the turbulence dynamics results from the dynamics that cause the changes in pressure–strain rate correlations discussed in § 7.

Although energy moves on average from the turbulence to the polymer, figure 16 shows that, locally, energy moves in both directions as polymer both stretches and contracts. We plot p.d.f.s of fluctuating viscous dissipation rate $-\epsilon' = -2\nu_s s_{ij} s_{ji}$ and fluctuating polymer turbulent energy exchange $-\gamma' = -\tau^p_{ij} s_{ji}/\rho$ (see (2.13)). Although $-\gamma'$ has both positive and negative values, there is a clear dominance of negative $-\gamma'$ fluctuations with peak values more than three times the highest positive values. Locally as well as globally, there is a strong preference for polymer to extract energy from the turbulence.

The net rate of energy extracted from the turbulence (Γ) appears in the polymer energy budget equation (2.22) as a source of polymer elastic energy E_p. In figure 17 we compare elastic energy budget in HTSF at (*a*) lower and (*b*) higher resolutions and Reynolds numbers, for comparison with the channel flow simulations of (*c*) Ptasinski *et al.* (2003) and (*d*) Min *et al.* (2003*b*). The 128^3 HTSF simulations have a narrower range of We_S (1.4–10.6) whereas the 256^3 cover almost the entire range of We_S (1.4–85) found in lower and higher DR channel flow simulations (figure 1). As discussed in § 7, mean shear becomes the dominant contributor to polymer stretch when the turbulence has moved from the low-DR regime I into the high-DR regime II and into MDR. Correspondingly, figure 17(*b*) shows that the production of polymer energy P_p by mean shear rate overtakes polymer–turbulence energy exchange rate Γ in the transition from the low-DR regimes $\mathrm{I_a}$ to $\mathrm{I_b}$ and dominates the production of

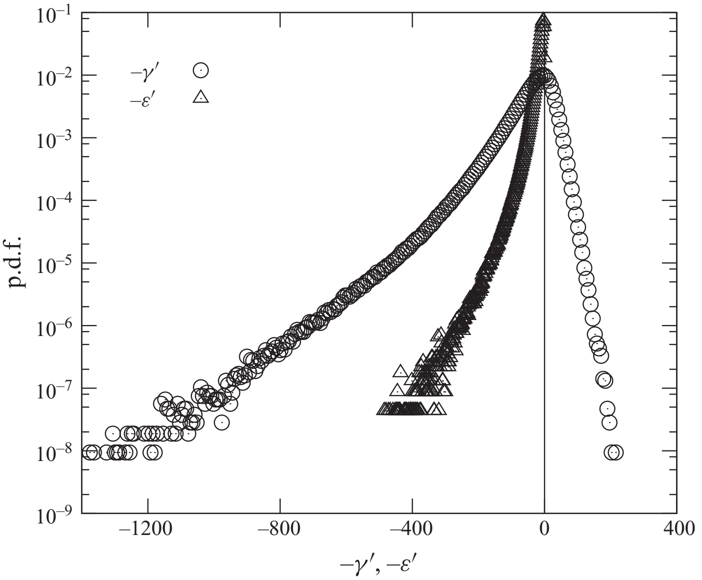

FIGURE 16. Probability density functions of fluctuating viscous dissipation rate $-\epsilon'$, and fluctuating polymer–turbulence energy exchange $-\gamma'$, for simulation 256D ($We_S = 3.5$, $1 - \beta = 0.05$, table 1).

elastic energy at higher We_S in regimes II and III. The net rate of polymer energy production $P_p + \Gamma$ roughly balances the rate of polymer energy dissipation $-\epsilon_p$, providing a second route for the transfer of TKE to internal energy.

In a manner similar to figure 9, in figure 17 we compare the elastic energy budget from HTSF with the channel flow DNS for lower Weissenberg numbers in (*a*) and (*c*) and higher Weissenberg numbers in (*b*) and (*d*). The comparisons between HTSF and channel flow are in excellent qualitative agreement outside the viscous sublayer of the channel flow, adding additional overall correspondence between the polymer turbulence physics in an unbounded HTSF and wall-bounded channel flow.

9. Conclusions

We modelled the elastic layer of the polymer-laden drag reducing turbulent boundary layer with the polymer-laden HTSF and compared HTSF predictions with channel flow experiments and simulations. Comparison with the experiments showed excellent qualitative agreement, and the many comparisons we made between HTSF and channel flow simulations show that the homogeneous shear flow captures the trends of different statistics essential to polymer–turbulence interactions within the elastic layer qualitatively and even quantitatively. The most important conclusion from these detailed comparisons is that the physics underlying polymer DR is not directly associated with the interactions between the inertial and viscous layers adjacent to the wall. Although there is no question that the addition of a polymer leads to important changes in the near-wall structure, the analysis in this study of a polymer-laden wall-free HTSF indicates that the essential mechanisms underlying polymer drag reduction originate from the interactions among turbulence fluctuations, polymer molecules and mean shear in the elastic layer above the viscous sublayer that lead to the suppression of momentum flux from above to the wall below.

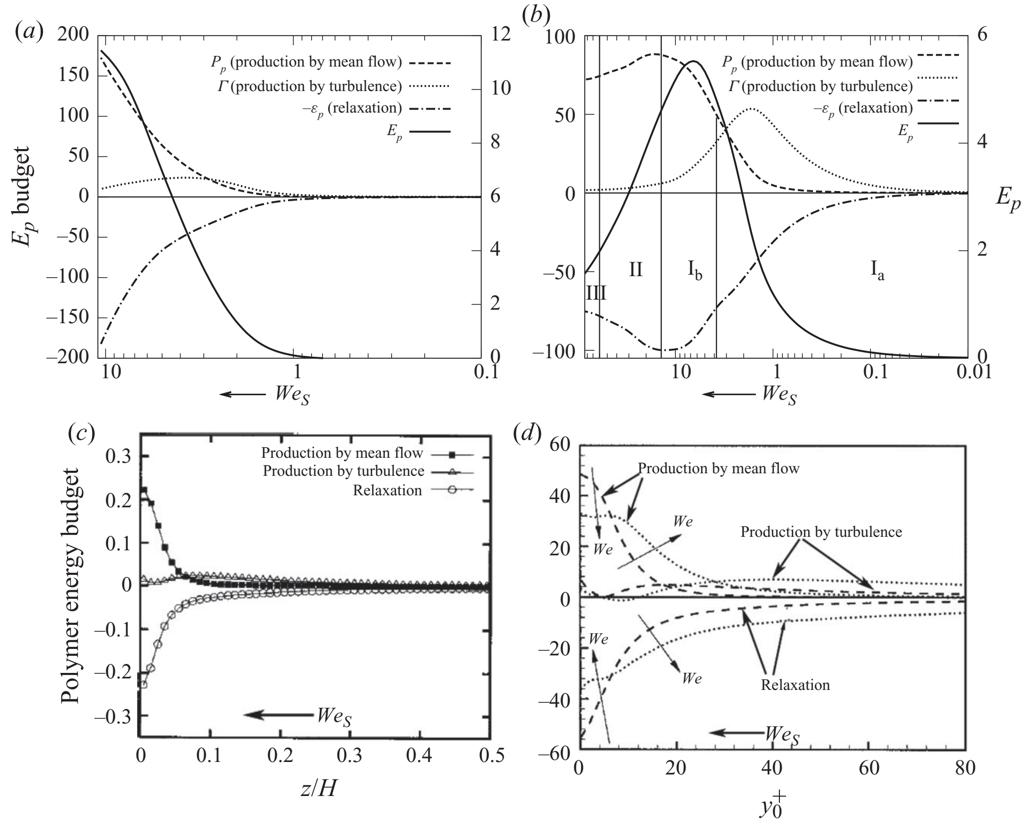

FIGURE 17. (*a*, *b*) Elastic energy, E_p (right axis) and the terms (left axis) in the budget for polymer elastic energy (see (2.22)), with increasing Weissenberg number We_S, in the equilibrium state for (*a*) 128^3; (*b*) 256^3 HTSF simulations. (*c*, *d*) Elastic energy E_p balance with increasing $y^+ = 0$ in channel flow for a comparison with HTSF, (*c*) Ptasinski *et al.* (2003) and (*d*) Min *et al.* (2003*b*). We_S increases as the wall is approached ($y^+ = 0$), as shown in figure 1.

Using the relative reduction in total stress to quantify %*DR*, we showed that HTSF exhibited low- and high-DR regimes, as well as an asymptotic regime similar to the MDR limit observed in experiments. We find that at very low Weissenberg number and concentrations, the ‘incipient’ state when the polymer effect is first deviating from the Newtonian state, the turbulence is highly sensitive to increasing polymer effect. We argue that the increase in streamwise velocity variance that has been measured in channel flow experiments and simulations in the low-DR regime is an indirect consequence of the suppression of turbulent momentum flux through the elastic layer, causing an increase in mean shear there, and not a primary mechanism of drag reduction. This high sensitivity at very low Weissenberg numbers and concentrations disappears rapidly as polymer influence increases and the turbulence moves out of the low-DR into the high-DR state. In the high-DR state, the entire Reynolds stress tensor is suppressed with increasing %*DR*, including streamwise velocity variance, consistent with the HTSF predictions, and mean shear rate takes over from fluctuating strain rate as the dominant mechanism that maintains polymer stretch.

The HTSF simulations show how the suppression of Reynolds shear stress that underlies drag reduction results from the suppression of vertical velocity fluctuations by the polymer. Except for very low Weissenberg numbers, the suppression of vertical velocity variance follows from a polymer-induced suppression of slow pressure–strain rate correlations, where polymer preferentially suppresses the inter-component transfer of energy into vertical velocity fluctuations. In the high-Weissenberg-number MDR limit, slow pressure–strain rate energy transfer to vertical velocity fluctuations becomes smaller than the rapid pressure–strain rate energy transfer out of them so that the Newtonian route to the maintenance of vertical velocity fluctuations and turbulence shuts down. In this MDR-like asymptotic state, vertical velocity fluctuations are maintained by the polymer pressure–strain rate inter-component energy transfer from the transverse component. Our analysis of the homogeneous polymer-laden shear turbulence suggests that MDR is an extremely unusual turbulence state that would re-laminarize if it were not for the maintenance of a low level of vertical velocity fluctuations by interactions between polymer, turbulence and mean shear that manifest as a polymer contribution to polymer pressure–strain rate correlations. Interestingly, this polymer contribution transfers energy into vertical velocity from spanwise fluctuations rather than the streamwise fluctuations with the Newtonian route.

The important conclusion from this study is that only three essential ingredients underlie the essence of polymer DR: turbulence, polymer and mean shear rate. The HTSF simulations demonstrate how in equilibrium the statistical structure of sheared turbulence is rapidly altered by low levels of polymer effect, how the Newtonian turbulence transitions to a highly non-Newtonian state at moderate levels of polymer effect and how the turbulence reaches a highly unusual asymptotic state of MDR without re-laminarization. At low polymer effect, polymer–turbulence interactions are in direct competition with classical Newtonian turbulence dynamics and small changes in polymer time scale or concentration lead to major alterations in turbulence dynamics. At high polymer effect, the sheared turbulence is highly non-classical with nearly depleted small-scale strain-dominated scales and the maintenance of the much-altered large-scale turbulence by a combination of mean shear and polymer interacting symbiotically with the remaining large-scale turbulence fluctuations.

We show that the polymer-laden HTSF is a good model for the suppression of momentum flux through the elastic layer of the polymer-laden turbulent boundary layer. Our analysis suggests that the elastic layer is a consequence of the sensitivity of a polymer-laden sheared turbulence to the shear Weissenberg number $We_S = \lambda_p S$. We have shown that We_S increases towards the wall as a consequence of shear rate scaling roughly like $1/y$ in the surface layer. Thus, since frictional forces suppress fluctuations adjacent to the surface, the strongest levels of polymer–turbulence suppression of momentum flux occur in the inertial region directly outside the friction-dominated wall layer, traditionally the upper buffer layer and lower inertial surface layer where We_S is maximal. Our study indicates that polymer DR results from the suppression of momentum flux off the surface in the lower shear-dominating inertial wall layer which, at higher DR, appears as an ‘elastic’ log layer. In this way, polymer can reduce surface shear stress equally in both smooth and rough wall boundary layers.

We are very grateful to Professor Anthony N. Beris and Dr Kostas D. Housiadas for providing us with the data from their channel flow simulations and Dr Kostas D. Housiadas for helpful discussion. This work has also benefited from many fruitful discussions with Drs Ronald Larson, Richard Leighton, David Walker and Howard Petrie. We are grateful for financial support from the Defense Advanced Research Projects Agency (DARPA) through the Friction Drag Reduction program under grants MDA972-01-C-0032 and HR0011-04-C0010 (subcontract). We are also grateful to High Performance Computing Group at The Pennsylvania State University for providing computing resources and we are particularly grateful to Jason Holmes and Jeff Nucciarone for providing substantial help in running our simulations. The first author is also grateful for support from the Department of Mechanical Engineering at The Pennsylvania State University during interim periods.

REFERENCES

de Angelis, E., Casciola, C. M., Benzi, R. & Piva, R. 2005 Homogeneous isotropic turbulence in dilute polymers. *J. Fluid Mech.* **531**, 1–10.

Bird, R. B., Curtiss, C. F., Armstrong, R. C. & Hassager, O. 1987 *Dynamics of Polymeric Liquids*, 2nd edn, vol. 2. John Wiley.

Brasseur, J. G. & Lin, W. 2005 Kinematics and dynamics of small-scale vorticity and strain-rate structures in the transition from isotropic to shear turbulence. *Fluid Dyn. Res.* **36**, 357–384.

Casciola, C. M., Gualtieri, P., Jacob, B. & Piva, R. 2005 Scaling properties in the production range of shear dominated flows. *Phys. Rev. Lett.* **95**, 024503.

Dimitropoulos, C. D., Dubief, Y., Shaqfeh, E. S. G., Moin, P. & Lele, S. K. 2005 Direct numerical simulation of polymer-induced drag reduction in turbulent boundary layer flow. *Phys. Fluids* **17**, 011705.

Dimitropoulos, C. D., Sureshkumar, R. & Beris, A. N. 1998 Direct numerical simulation of turbulent channel flow exhibiting drag reduction: effect of the variation of rheological parameters. *J. Non-Newton. Fluid Mech.* **79**, 433–468.

Dimitropoulos, C. D., Sureshkumar, R., Beris, A. N. & Handler, R. A. 2001 Budgets of Reynolds stress, kinetic energy and streamwise enstrophy in viscoelastic turbulent channel flow. *Phys. Fluids* **13**, 1016–1027.

Dubief, Y., White, C. M., Terrapon, V. E., Shaqfeh, E. S. G., Moin, P. & Lele, S. K. 2004 On the coherent drag-reducing and turbulent-enhancing behaviour of polymers in wall flows. *J. Fluid Mech.* **514**, 271–280.

Dupret, F. & Marchal, J. M. 1986 Loss of evolution in the flow of viscoelastic fluid. *J. Non-Newton. Fluid Mech.* **20**, 143–171.

de Gennes, P. G. 1990 *Introduction to Polymer Dynamics*. Cambridge University Press.

George, W. K., Beuther, P. D. & Arndt, R. E. A. 1984 Pressure spectra in turbulent free shear flows. *J. Fluid Mech.* **148**, 155–191.

Gyr, A. & Bewersdorff, H.-W. 1995 *Drag Reduction of Turbulent Flows by Additives*, 1st edn. Kluwer.

Harder, K. J. & Tiederman, W. G. 1991 Drag reduction and turbulent structure in two-dimensional channel flows. *Phil. Trans. R. Soc. Lond.* **336**, 19–34.

Housiadas, K. D. & Beris, A. N. 2003 Polymer-induced drag reduction: effects of the variations in elasticity and inertia in turbulent viscoelastic channel flow. *Phys. Fluids* **15**, 2369–2384.

Housiadas, K. D. & Beris, A. N. 2005 Direct numerical simulations of viscoelastic turbulent channel flows at high drag reduction. *Korean–Aust. J. Rheol.* **17**, 131–140.

Hoyt, J. W. 1971 Effect of additives on fluid friction. *Trans. ASME J. Basic Engng* **94**, 258–285.

Ilg, P., de Angelis, E., Karlin, I. V., Casciola, C. M. & Succi, S. 2002 Polymer dynamics in wall turbulent flow. *Europhys. Lett.* **58**, 616–622.

Jin, S. & Collins, L. R. 2007 Dynamics of dissolved polymer chains in isotropic turbulence. *New J. Phys.* **9**, 360.

Keunings, R. 1997 On the Peterlin approximation for finitely extensible dumbbells. *J. Non-Newton. Fluid Mech.* **68**, 85–100.

Khanna, S. 1995 Structure of the atmospheric boundary layer from large eddy simulations. PhD thesis, Department of Mechanical Engineering, The Pennsylvania State University, University Park, PA.

Kim, J. & Lee, M. J. 1989 The structure of pressure fluctuations in turbulent shear flows. In *Seventh Symposium on Turbulent Shear Flows*, Stanford University, CA (ed. F. Durst, B. E. Launder, F. W. Schmidt & J. H. Whitlaw), pp. 1.1.1–1.1.6. Standford University.

KIM, J. & MOIN, P. 1986 The structure of the vorticity field in turbulent channel flow. Part 2. Study of ensemble-averaged fields. *J. Fluid Mech.* **162**, 339–363.

KURGANOV, A. & TADMOR, E. 2000 New high-resolution central schemes for nonlinear conservation laws and convection–diffusion equations. *J. Comput. Phys.* **160**, 241–282.

LANDAHL, M. T. 1973 Drag reduction by polymer addition. In *Proceedings of the 13th International Congress on Theoretical and Applied Mechanics*, Moscow, Russia (ed. E. Becker & G. K. Mikhailov), pp. 177–179. Springer.

LARSON, R. G. 1999 *The Structure and Rheology of Complex Fluids*, 1st edn. Oxford University Press.

LEE, M. J. 1985 Numerical experiments on the structure of homogeneous turbulence. PhD thesis 24, Department of Mechanical Engineering, Stanford University, Stanford, CA.

LEE, M. J., KIM, J. & MOIN, P. 1990 Structure of turbulence at high shear rate. *J. Fluid Mech.* **216**, 561–583.

LIAW, G. C., ZAKIN, J. L. & PATTERSON, G. K. 1971 Effects of molecular characteristics of polymers on drag reduction. *AIChE J.* **17**, 391–397.

LO, T. S., L'VOV, V. S., POMYALOV, A. & PROCACCIA, I. 2005 Estimating von Kármán's constant from homogeneous turbulence. *Europhys. Lett.* **72** (6), 943–949.

LUMLEY, J. L. 1969 Drag reduction by additives. *Annu. Rev. Fluid Mech.* **1**, 367–384.

LUMLEY, J. L. 1973 Drag reduction in turbulent flow by polymer additives. *J. Polym. Sci., Macromol. Rev.* **7**, 263–290.

L'VOV, V. S., POMYALOV, A., PROCACCIA, I. & TIBERKEVICH, A. 2004 Drag reduction by polymers in wall bounded turbulence. *Phys. Rev. Lett.* **92**, 244503-1–244503-4.

MCCOMB, W. 1990 *The Physics of Fluid Turbulence*, 1st edn. Oxford University Press.

MCCOMB, W. D. & RABIE, L. H. 1979 Development of local turbulent drag reduction due to nonuniform polymer concentration. *Phys. Fluids* **22**, 183–185.

MCCOMB, W. D. & RABIE, L. H. 1982 Local drag reduction due to injection of polymer solutions into turbulent flow in a pipe. *AIChE J.* **28**, 547–557.

MIN, T., YOO, J. Y. & CHOI, H. 2003*a* Maximum drag reduction in a turbulent channel flow by polymer additives. *J. Fluid Mech.* **492**, 91–100.

MIN, T., YOO, J. Y., CHOI, H. & JOSEPH, D. D. 2003*b* Drag reduction by polymer additives in a turbulent channel flow. *J. Fluid Mech.* **486**, 213–238.

NIEUWSTADT, F. T. M. & DEN TOONDER, J. M. J. 2001 Drag reduction by polymer additives: a review. In *Turbulence Structure and Motion* (ed. A. Sooldati & R. Monti), pp. 269–316. Springer.

PETERLIN, A. 1966 Turbulent structure in low-concentration drag-reducing channel flows. *J. Polym. Sci.* B, *Polym. Lett.* **4**, 287–291.

PINHO, F. T. & WHITELAW, J. H. 1990 Flow of non-Newtonian fluids in a pipe. *J. Non-Newton. Fluid Mech.* **34**, 129–144.

PTASINSKI, P. K., BOERSMA, B. J., NIEUWSTADT, F. T. M., HULSEN, M. A., VAN DEN BRULE, B. H. A. A. & HUNT, J. C. R. 2003 Turbulent channel flow near maximum drag reduction: simulations, experiments and mechanisms. *J. Fluid Mech.* **490**, 251–291.

PTASINSKI, P. K., NIEUWSTADT, F. T. M., VAN DEN BRULE, B. H. A. A. & HULSEN, M. A. 2001 Experiments in turbulent pipe flow with polymer additives at maximum drag reduction. *Flow, Turbulence Combust.* **66**, 159–182.

ROGALLO, R. S. 1981 Numerical experiments in homogeneous turbulence. *Tech. Rep.* TM 81315. NASA.

ROGERS, M. M. & MOIN, P. 1987 The structure of the vorticity field in homogeneous turbulent shear flow. *J. Fluid Mech.* **176**, 33–66.

SPANGLER, J. G. 1969 Studies of viscous drag reduction with polymers including turbulence measurements and roughness effects. In *Viscous Drag Reduction* (ed. C. S. Wells), pp. 131–155. Plenum.

SURESHKUMAR, R. & BERIS, A. N. 1995 Effect of artificial stress diffusivity on the stability of numerical calculations and the flow dynamics of time-dependent viscoelastic flows. *J. Non-Newton. Fluid Mech.* **60**, 53–80.

SURESHKUMAR, R. & BERIS, A. N. 1997 Simulation of time-dependent viscoelastic channel Poiseuille flow at high Reynolds numbers. *Chem. Engng Sci.* **51**, 1451–1471.

Sureshkumar, R., Beris, A. N. & Handler, R. A. 1997 Direct numerical simulation of turbulent flow of a polymer solution. *Phys. Fluids* **9**, 743–755.

Tabor, M. & de Gennes, P. G. 1986 A cascade theory of drag reduction. *Europhys. Lett.* **2**, 519–522.

Toms, B. A. 1949 Some observations on the flow of linear polymer solutions through straight tubes at large Reynolds numbers. In *Proceedings of the 1st International Congress on Rheology*, vol. 2, pp. 135–141, North Holland, Amsterdam.

den Toonder, J. M. J., Hulsen, M. A., Kuiken, G. D. C. & Nieuwstadt, F. T. M. 1997 Drag reduction by polymer additives in a turbulent pipe flow: numerical and laboratory experiments. *J. Fluid Mech.* **337**, 193–231.

Vaithianathan, T. & Collins, L. R. 2003 Numerical approach to simulating turbulent flow of a viscoelastic polymer solution. *J. Comput. Phys.* **187**, 1–21.

Vaithianathan, T., Robert, A., Brasseur, J. G. & Collins, L. R. 2006 An improved algorithm for simulating three-dimensional, viscoelastic turbulence. *J. Non-Newton. Fluid Mech.* **140**, 3–22.

Vaithianathan, T., Robert, A., Brasseur, J. G. & Collins, L. R. 2007 Polymer mixing in shear-driven turbulence. *J. Fluid Mech.* **585**, 487–497.

Virk, P. S. 1971*a* Drag reduction in rough pipes. *J. Fluid Mech.* **45**, 225–246.

Virk, P. S. 1971*b* An elastic sublayer model for drag reduction by dilute solutions of linear macromolecules. *J. Fluid Mech.* **45**, 417–440.

Virk, P. S. 1975 Drag reduction fundamentals. *AIChE J.* **21**, 625–656.

Walker, D. T. & Tiederman, W. G. 1990 Turbulent structure in a channel flow with polymer injection at the wall. *J. Fluid Mech.* **218**, 377–403.

Warholic, M. D., Massah, H. & Hanratty, T. J. 1999 Influence of drag-reducing polymers on turbulence: effects of Reynolds number, concentration and mixing. *Exp. Fluids* **27**, 461–472.

Warner, H. R. 1972 Kinetic theory and rheology of dilute suspensions of finitely extensible dumbbell. *Ind. Engng Chem. Fundam.* **11**, 379–387.

Wei, T. & Willamarth, W. W. 1992 Modifying turbulent structure with drag-reducing polymer additives in turbulent channel flows. *J. Non-Newton. Fluid Mech.* **245**, 619–641.

White, C. M. & Mungal, M. G. 2008 Mechanics and prediction of turbulent drag reduction with polymer additives. *Annu. Rev. Fluid Mech.* **40**, 235–256.

Willamarth, W. W., Wei, T. & Lee, C. 1987 Laser anemometer measurement of Reynolds stress in a turbulent channel flow with drag reducing polymer additives. *Phys. Fluids* **30**, 933–935.

Wu, J. 1969 Drag reduction in external flows of additive solution. In *Viscous Drag Reduction* (ed. C. S. Wells), pp. 331–350. Plenum.

Wu, J. & Tulin, M. 1972 Drag reduction by ejecting additive into pure-water boundary layer. *Trans. ASME J. Basic Engng* **94**, 749–756.